The Astrophysical Journal, 716:1217–1240, 2010 June 20 doi:10.1088/0004-637X/716/2/1217

EXPLORING THE SMALL MAGELLANIC CLOUD TO THE FAINTEST X-RAY FLUXES: SOURCE CATALOG, TIMING, AND SPECTRAL ANALYSIS

Silas Laycock[1], Andreas Zezas[2,3,4], Jaesub Hong[2], Jeremy J. Drake[2], and Valsamo Antoniou[2,3]
[1] Gemini Observatory, 670 North A'ohoku Place, Hilo, HI 96720, USA
[2] Harvard-Smithsonian Center for Astrophysics, 60 Garden Street, Cambridge, MA 02138, USA
[3] Physics Department, University of Crete, 71003 Heraklion, Greece
[4] IESL, Foundation for Research and Technology, 71110 Heraklion, Greece
Received 2008 September 9; accepted 2010 April 20; published 2010 May 28

ABSTRACT

We present the results of a pair of 100 ks *Chandra* observations in the Small Magellanic Cloud (SMC) to survey high-mass X-ray binaries (HMXBs), stars, and low-mass X-ray binaries (LMXBs)/cataclysmic variables down to $L_x = 4.3 \times 10^{32}$ erg s^{-1}. The two SMC Deep Fields (DFs) are located in the most active star-forming region of the bar, with Deep Field-1 positioned at the most pulsar-rich location identified from previous surveys. Two new pulsars were discovered in the outburst: CXOU J004929.7-731058 ($P = 892$ s), CXOU J005252.2-721715 ($P = 326$ s), and three new HMXB candidates were identified. Of the 15 Be-pulsars now known in the field, 13 were detected, with pulsations seen in 9 of them. Ephemerides demonstrate that 6 of the 10 pulsars known to exhibit regular outbursts were seen outside their periastron phase, and quiescent X-ray emission at $L_X = 10^{33}$–10^{34} erg s^{-1} is shown to be common. Comparison with *ROSAT*, *ASCA,* and *XMM-Newton* catalogs resulted in positive identification of several previously ambiguous sources. Bright optical counterparts exist for 40 of the X-ray sources, of which 33 are consistent with early-type stars ($M_V < -2$, $B-V < 0.2$), and are the subject of a companion paper. The results point to an underlying HMXB population density up to double that of active systems. The full catalog of 394 point sources is presented along with detailed analyses of timing and spectral properties.

Key words: Magellanic Clouds – stars: emission-line, Be – stars: neutron – X-rays: binaries

Online-only material: machine-readable table

1. INTRODUCTION

The Small Magellanic Cloud (SMC) has proven to be an incomparable laboratory for astrophysics. The SMC is one of the dwarf irregular satellites of the Milky Way, and unlike most other members of that group (excepting the LMC) it is experiencing an era of intense star formation. The star formation rate (SFR) of the SMC is in the range 0.05–0.4 $M_\odot$ yr^{-1} (Harris & Zaritsky 2004; Shtykovskiy & Gilfanov 2005), where the upper bound is about 150 times greater than for the Milky Way. Situated in a part of the sky unobstructed by the galactic plane, the SMC affords a ringside seat to the unfolding drama. The combination of low extinction ($N_{\rm H} \sim 10^{21}$ cm^{-2}) and a small depth/size in relation to its distance from earth ($D_{\rm SMC} = 60$ kpc; Hilditch et al. 2005) effectively puts the entire population at a common distance. A substantial fraction of the SMC can be observed simultaneously thanks to its compact size, which facilitates population studies. The recent star formation episode in the SMC has led to a large population of massive stars and high-mass X-ray binaries (HMXBs) which are the relics of the short-lived upper end of the initial mass function. The young population and the majority of the known X-ray binaries (XRBs) are concentrated in the SMC's Bar.

HMXB pulsars are rotating neutron stars (NSs) in binary systems with Be-type (spectral type 09-B2, luminosity classes V–III) or supergiant stellar companions. Most HMXBs are of the Be type which account for 70% in the Milky Way and $\geqslant$98% in the SMC (Coe et al. 2005). The Be-star equatorial disk provides a reservoir of matter that can be accreted onto the NS during periastron passage (most known systems have large orbital eccentricity) or during large-scale disk ejection episodes. This scenario leads to strings of X-ray outbursts with typical luminosities $L_X \sim 10^{36}$–10^{37} erg s^{-1}, spaced at the orbital period, plus infrequent giant outbursts of greater duration and luminosity (see Negueruela 1998 for a review).

Monitoring surveys of the SMC with, e.g., *RXTE* (Laycock et al. 2005, hereafter L05; Galache et al. 2008, hereafter G08) see X-ray pulsars in outburst at $>10^{36}$ erg s^{-1} and have counted $\sim$50 to date. The above scenario suggests most X-ray binary (XRB) pulsars spend the majority of the time in quiescence. In order to enumerate the overall population, it is necessary to observe and count X-ray pulsars in their low-luminosity state as well. The *ROSAT* and *ASCA* missions detected many faint X-ray point sources (e.g., Haberl & Sasaki 2000), but the typical positional uncertainties frequently made positive identification difficult. Recent studies using *XMM-Newton* (Haberl et al. 2008; Haberl & Pietsch 2004) and *Chandra* (Antoniou et al. 2009; Edge et al. 2004) have now pinpointed the optical counterparts of many of these HMXBs. The literature contains measurements of many previously unidentified X-ray sources (e.g., from *ROSAT* and *ASCA*) that can now be localized, to provide a valuable historical record of variability which is a hallmark of XRBs, even in the absence of pulsations. For this study, we targeted the most densely populated regions of the SMC Bar with sufficient sensitivity (10^{33} erg s^{-1}) to detect quiescent HMXB systems with good positional accuracy.

XRBs with large circular orbits, and those containing fast-rotating NSs, do not fit the classic pattern of periodic activity, due to the generally low luminosity of the former and the infrequent occurrence of outbursts in the latter. In systems with low eccentricity, no periastron-passage events can occur and the Be-star disk remains tidally truncated well within the orbital radius of the NS (Okazaki & Negueruela 2001). It is widely recognized that accretion onto the magnetic NS faces a

Table 1
Chandra Observations

Field	ObsID	Aim Point R.A., Decl.	Roll (deg)	Start UT	MJD	Exposure ($\times 10^3$ s)
DF1	7155	00:53:34.50, −72:26:43.20	161	2006 Apr 25 05:32	53850.23	50
	7327	00:53:34.50, −72:26:43.20	161	2006 Apr 26 15:14	53851.63	50
DF2	8479	00:50:41.40, −73:16:10.30	317	2006 Nov 21 12:21	54060.51	45
	7156	00:50:41.40, −73:16:10.30	317	2006 Nov 22 19:06	54061.80	39
	8481	00:50:41.40, −73:16:10.30	317	2006 Nov 23 16:06	54062.67	16

centrifugal barrier that scales rapidly with spin frequency (see, e.g., Frank et al. 2002). Fast-rotating pulsars remain in the so-called propellor regime (Illarionov & Sunyaev 1975) until the mass-transfer rate from their companion exceeds the barrier or threshold value (e.g., Campana et al. 2001). For spin periods below ∼10 s, the resulting accretion-powered luminosity is $>10^{38}$ erg s^{-1} and such outbursts occur only rarely.

The primary aim of our deep (100 ks) *Chandra* survey is to provide a complete census of XRBs with greatly reduced luminosity bias compared to the existing sample within a limited survey region. Stellar population synthesis models will greatly benefit from hard numbers upon which to base the relative probabilities of various evolutionary paths. For example, in modeling the supernovae that occur in the formation of XRBs, one needs to reproduce the actual distribution of orbital periods and eccentricities. If current catalogs underrepresent systems with large orbital separations and low eccentricity, the input to these models will be flawed.

A second motivation of the Deep Fields (DFs) project is to investigate the apparently universal correlation between SFR and the integrated luminosity of HMXB found by Grimm et al. (2003). The absolute number normalization of this relationship remains unknown for two reasons. Sufficiently faint fluxes have not been probed to discover the underlying numbers of HMXBs, and the transient nature of most HMXBs makes it difficult to determine the total population. Shtykovskiy & Gilfanov (2005) found that although the number of HMXBs in the SMC fits the Grimm et al. (2003) relation based on optical estimates of SFR, if Hα, FIR, and UV indicators are used instead, HMXBs are overabundant by up to a factor of 10 compared to the Milky Way.

We present the complete X-ray source catalog as an electronic table accompanying this paper. We describe below in detail the properties of the brightest sources, and an analysis of the timing and spectral properties of the sample, focusing on X-ray pulsars and sources coincident with known objects. An optical survey is being conducted in parallel (V. Antoniou et al. 2010, in preparation; hereafter VA10) to enable more robust and complete classifications of XRBs, cataclysmic variables (CVs), stellar coronae, and background active galactic nuclei (AGNs). The further goals of this project are as follows and are being pursued in a series of forthcoming papers.

1. Classify all the sources by finding and studying their optical counterparts. Discriminating the different source classes is a requisite for aims 3–5 below. Our optical survey is being carried out in parallel with the X-ray survey using the *Hubble Space Telescope* and Magellan 6.5 m telescope. With high resolution imaging/photometry to $R, I < 26$, we will be able to independently classify the optical counterparts to most of the sample. The optical counterpart identifications will enable items 2–4.
2. Construct the luminosity distribution down to faint X-ray fluxes. This will test whether multiple point-source populations may be present, versus a monolithic HMXB ensemble.
3. Search for coronal X-ray emission from the most active stars in the SMC.
4. Constrain the incidence of low-mass X-ray binaries (LMXBs) and CVs in the SMC. CVs should be present throughout the SMC which is dominated by an old population of red giants. Outbursts (novae and dwarf novae) are extremely infrequent and fainter in X-rays than HMXBs. Thus, they will be harder to find. No LMXBs or CVs are known in the SMC, and extrapolation from the total mass in stars predicts only a handful of LMXBs, thus an observational constraint (or positive discoveries of LMXB) will provide important input to population synthesis models.

2. OBSERVATIONS AND DATA REDUCTION

The two SMC fields (Table 1) are located in the most active star-forming region of the Bar. Each field was observed for a total of 100 ks with *Chandra*'s Advanced CCD Imaging Spectrometer (ACIS), as detailed in Table 1. For mission operational reasons, the observations could not be scheduled as contiguous blocks, a circumstance anticipated in advance. Deep Field-1 (DF1) was observed in two observations of ∼50 ks each, over the course of two days. Deep Field-2 (DF2) was split into three observations spread over three days. The spacecraft aim point and roll angle were identical for the observations making up each field, so as to simplify the data reduction. The ACIS-I array was selected for its large ($16' \times 16'$) contiguous square field imaged by four front-illuminated CCDs (I0–I3). Two of the "S" array CCDs (S5, S6) were also active. Timed exposure, faint mode was used with the default "most-efficient" frame time of 3.2 s and the unfiltered energy range (0.1–15 keV).

DF1 is positioned at the most pulsar-rich location identified from previous surveys. The DF1 coordinates also coincide with the primary position used by the *RXTE* monitoring program (L05), for weekly pulsar observations of 5–10 ks duration for the past 10 years, DF2 was also frequently observed by *RXTE*. Figure 1 shows all *Chandra* observations in the SMC Bar, which was targeted by an earlier Shallow survey (Taylor et al. 2003; Antoniou et al. 2009). DF1 and DF2 were previously observed as Field-5 and Field-4 of the Shallow survey. The earlier observations were 10 ks ACIS-I observations which discovered the pulsars SXP503 and SXP138 (Edge et al. 2004) and a bright supernova remnant (SNR; Taylor et al. 2003) coincident with the *ROSAT* source PSPC 461= HRI 38 (Sasaki et al. 2000).

The data were stacked and reduced using the processing pipeline developed at CfA for the *Chandra* Multi-wavelength Project (ChaMP, Kim et al. 2004 and ChaMPlane, Hong et al. 2005). The pipeline performs all standard *Chandra* calibrations and corrections including Good Time Interval filtering, exposure map correction, cosmic-ray afterglow removal, aspect solution, charge-transfer inefficiency, effective area, and time-dependent

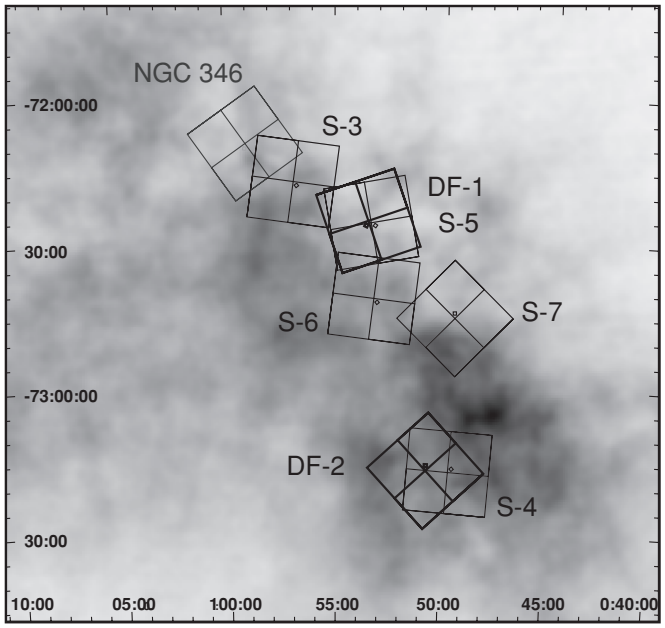

Figure 1. *Chandra* observations in the SMC Bar. The 100 ks fields presented in this paper are labeled as DF1 and DF2. The Shallow (10 ks) survey of Antoniou et al. (2009) is S-3–7, and the SMC open cluster NGC 346 (100 ks) observed by Naze et al. (2004) is shown in gray. Outlines of the four ACIS-I CCDs are plotted, with the appropriate roll angle, and the *Chandra* aim point is marked. Background is the Stanimirovic et al. (1999) H I image.

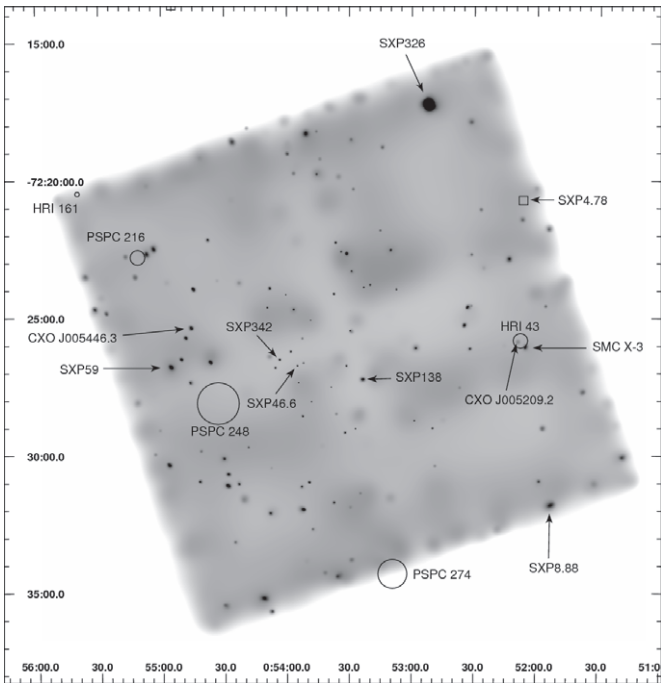

Figure 2. Adaptively smoothed broadband (0.3–8 keV) *Chandra* image of DF1, showing locations of pulsars, HMXB candidates, and unidentified *ROSAT* sources. The ACIS-I field measures $16' \times 16'$ on each side. The many unidentified point sources are a mixture of quiescent XRBs (17 *Chandra* sources in this field have bright ($V < 17$) optical counterparts), stars, and background AGNs.

energy response (due to contaminant buildup on the ACIS optical blocking filter). Source detection was performed with the *wavdetect* algorithm, on images extracted in three energy bands (Bx = 0.3–8 keV, Sx = 0.3–2.5 keV, and Hx = 2.5–8 keV) at spatial scales of 1, 2, 4, 8, and 16 pixels. X-ray source properties were measured using the aperture photometry procedure described by Hong et al. (2005), which accounts for neighboring sources with overlapping source or background regions. The full position-dependent instrument sensitivity is accounted for by application of the exposure maps and response matrices (RMFs and ARFs) generated by the ChaMP pipeline. Positional error circles are assigned to each source based on net counts and distance from the aim point, according to the standard model of Hong et al. (2005) which is based on detailed simulations of the full *Chandra* optical path and ACIS characteristics. Source detection and photometry were performed both on the individual exposures in Table 1 and the complete stacked data set for each field. The resulting object lists were then combined to yield a catalog of unique sources, with the best measurement of each source used to define its coordinates and error circle. In nearly all cases, the stacked Bx image provided the best measurement with the exception of variable sources which may be detected at better signal-to-noise ratio (S/N) in a particular observation, and particularly hard or soft sources which may achieve the best S/N in the Sx or Hx images.

We present the full list of detected sources on the ACIS-I array in Table 2 of the online version of this journal. The print edition contains a subset of sources ranked by S/N, cut to exclude sources with S/N < 10. The catalog lists coordinates, error radii (95% statistical error), X-ray fluxes in three conventional energy bands (*Bc* 0.5–8.0 keV, *Sc* 0.5–2.0 keV, and *Hc* 2.0–8.0 keV), and energy Quantiles. The energy bands are chosen to match the convention used for *ROSAT*, and quantiles were generated according to the definitions of Hong et al. (2004). Background subtraction is applied to each source, to compute net counts, by subtracting the count rate in an annular sky region surrounding the source extraction region. The aperture photometry routine uses extraction regions tied to the (spatially varying) 90% encircled energy radius, which results in slightly different count rates than are reported by *wavdetect*.

The flux values in Table 2 are generated using a varying spectral model, whose parameters are selected according to the quantile value for each source. This approach is introduced by Hong et al. (2009) and frees the flux estimation from systematic errors inherent in assuming a single spectral model for all sources. The electronic version of Table 2 also contains flux values derived for fixed power law ($\Gamma = 1.4$) and thermal plasma ($kT = 1$ keV) spectral models. The quantile-based fluxes are derived from one of three power-law models that are defined by the natural groupings of sources in the quantile diagram (cf. Section 7.3). The group to which each source is assigned for flux calculation is given in Table 2. For field DF1, the models are: group 1: $N_{\rm H} = 2.8$, $\Gamma = 2.35$, group 2: $N_{\rm H} = 2.5$, $\Gamma = 1.42$, and group 3: $N_{\rm H} = 20.0$, $\Gamma = 1.52$ (absorption column density in units of 10^{21} cm^{-2}). For field DF2, the models are similar: group 1: $N_{\rm H}$=0.6, $\Gamma = 2.94$, group 2: $N_{\rm H} = 4.9$, $\Gamma = 1.38$, and group 3: $N_{\rm H} = 27.0$, $\Gamma = 1.91$. In both fields, the algorithm identifies quantitatively similar groupings, corresponding to a very soft spectrum with typical (or sub) SMC absorption (group 1), a hard XRB-like spectrum with SMC absorption (group 2), and a heavily absorbed AGN-like spectrum (group 3). The two fixed models are provided as they will be more accurate if the nature of an individual source is known by other means.

In Figures 2 and 3, we present adaptively smoothed images of the stacked data for the two fields. After creating co-added, filtered level-2 event files, the broadband (0.3–8 keV) data were adaptively smoothed with the CIAO *csmooth* tool with the significance scale set to 3σ–5σ (resulting in minimum and

Table 2
Chandra SMC DFs Source Catalog

Name CXOU	R.A. (deg)	Decl. (deg)	$r95$ (arcsec)	F_{Bc} (0.5–8 keV)	F_{Sc} (0.5–2.0 keV) (10^{-14} erg cm^{-2} s^{-1})	F_{Hc} (2.0–8 keV)	E50 (keV)	Quantiles QDx	QDy	S/N
J005252.2-721715	13.217712	−72.287619	0.48	141.40 ± 1.52	23.92 ± 0.39	134.60 ± 1.92	2.37 ± 0.03	−0.43 ± 0.0077	1.03 ± 0.01	95.1
J004942.0-732314	12.425030	−73.387348	0.45	64.23 ± 1.04	7.62 ± 0.21	63.66 ± 1.28	2.85 ± 0.04	−0.31 ± 0.0093	1.06 ± 0.02	63.5
J005151.9-731033	12.966380	−73.176053	0.44	65.83 ± 1.21	11.03 ± 0.29	50.67 ± 1.32	2.01 ± 0.04	−0.55 ± 0.014	0.93 ± 0.02	57.1
J005044.6-731605	12.686208	−73.268118	0.29	32.68 ± 0.70	4.17 ± 0.15	31.07 ± 0.85	2.70 ± 0.07	−0.34 ± 0.017	1.02 ± 0.02	48.0
J004929.7-731058	12.374103	−73.182874	0.48	22.43 ± 0.63	2.38 ± 0.12	23.50 ± 0.80	2.98 ± 0.07	−0.27 ± 0.016	1.09 ± 0.02	37.3
J005323.8-722715	13.349580	−72.454326	0.30	30.00 ± 0.88	4.45 ± 0.22	31.22 ± 1.18	2.71 ± 0.08	−0.34 ± 0.02	0.98 ± 0.03	35.1
J004913.5-731138	12.306384	−73.193905	0.53	20.97 ± 0.65	2.23 ± 0.13	21.96 ± 0.82	2.91 ± 0.08	−0.29 ± 0.019	1.13 ± 0.03	33.7
J005057.1-731008	12.737953	−73.168905	0.46	11.00 ± 0.44	1.41 ± 0.09	10.42 ± 0.54	2.60 ± 0.10	−0.37 ± 0.026	1.02 ± 0.04	26.0
J004948.2-732211	12.451046	−73.369782	0.54	7.23 ± 0.36	1.32 ± 0.09	5.05 ± 0.39	1.86 ± 0.07	−0.6 ± 0.023	1.13 ± 0.05	20.7
J005437.1-722637	13.654878	−72.443838	0.41	4.21 ± 0.21	1.64 ± 0.10	2.93 ± 0.27	1.63 ± 0.04	−0.68 ± 0.018	1.25 ± 0.10	20.7
J005331.7-722240	13.382157	−72.378046	0.37	5.01 ± 0.27	1.20 ± 0.08	3.27 ± 0.29	1.73 ± 0.05	−0.64 ± 0.018	1.13 ± 0.08	19.6
J005456.1-722648	13.734005	−72.446703	0.50	5.59 ± 0.30	1.06 ± 0.08	4.82 ± 0.37	2.03 ± 0.17	−0.54 ± 0.052	0.94 ± 0.04	19.5
J005428.9-723107	13.620442	−72.518645	0.53	2.69 ± 0.17	1.36 ± 0.10	0.79 ± 0.16	1.25 ± 0.04	−0.85 ± 0.022	1.42 ± 0.07	16.6
J005215.4-731915	13.064582	−73.320960	0.61	4.86 ± 0.30	0.78 ± 0.07	3.88 ± 0.34	2.04 ± 0.15	−0.53 ± 0.048	0.95 ± 0.07	16.3
J005445.3-722358	13.688995	−72.399571	0.55	2.97 ± 0.23	0.70 ± 0.07	1.96 ± 0.26	1.68 ± 0.08	−0.66 ± 0.031	1.00 ± 0.08	13.7
J005352.4-723159	13.468608	−72.533165	0.53	2.46 ± 0.21	0.40 ± 0.05	2.41 ± 0.27	2.41 ± 0.17	−0.42 ± 0.048	1.13 ± 0.05	13.0
J004910.7-731717	12.294808	−73.288102	0.62	3.60 ± 0.30	0.07 ± 0.03	3.92 ± 0.34	3.82 ± 0.21	−0.075 ± 0.048	1.73 ± 0.07	13.0
J005337.8-722409	13.407884	−72.402501	0.35	3.53 ± 0.30	0.84 ± 0.09	2.30 ± 0.33	1.75 ± 0.07	−0.64 ± 0.026	1.14 ± 0.10	12.6
J005045.0-731539	12.687698	−73.261022	0.32	2.20 ± 0.19	0.46 ± 0.05	1.27 ± 0.19	1.64 ± 0.07	−0.68 ± 0.026	1.25 ± 0.10	12.3
J005153.2-723148	12.972059	−72.530146	0.95	3.02 ± 0.27	0.51 ± 0.07	2.86 ± 0.35	2.32 ± 0.20	−0.45 ± 0.057	1.06 ± 0.07	11.9
J005351.2-721818	13.463641	−72.305261	0.84	2.75 ± 0.24	0.73 ± 0.08	1.51 ± 0.26	1.58 ± 0.06	−0.7 ± 0.025	1.19 ± 0.13	11.6
J005446.3-722523	13.693035	−72.423111	0.56	2.14 ± 0.20	0.38 ± 0.05	1.93 ± 0.25	2.24 ± 0.22	−0.47 ± 0.062	1.28 ± 0.09	11.6
J005214.0-731918	13.058339	−73.321724	0.71	2.51 ± 0.23	0.33 ± 0.05	2.34 ± 0.28	2.40 ± 0.21	−0.42 ± 0.057	1.07 ± 0.09	11.5
J005457.2-723021	13.738400	−72.506080	0.76	2.18 ± 0.21	0.53 ± 0.06	1.40 ± 0.23	1.67 ± 0.13	−0.67 ± 0.049	1.18 ± 0.13	11.4
J005448.9-722544	13.704161	−72.429125	0.58	1.90 ± 0.18	0.53 ± 0.06	0.90 ± 0.18	1.54 ± 0.08	−0.72 ± 0.031	1.15 ± 0.15	11.3
J005411.5-723513	13.548300	−72.586961	1.00	1.75 ± 0.16	0.66 ± 0.08	1.28 ± 0.22	1.59 ± 0.08	−0.7 ± 0.033	1.30 ± 0.13	11.2
J004905.1-731411	12.271583	−73.236528	0.74	1.86 ± 0.23	0.34 ± 0.06	1.31 ± 0.22	1.94 ± 0.16	−0.57 ± 0.053	1.03 ± 0.15	11.1
J005235.0-722516	13.146195	−72.421379	0.47	1.76 ± 0.18	0.38 ± 0.05	1.31 ± 0.21	1.82 ± 0.16	−0.61 ± 0.054	1.08 ± 0.10	10.7
J005233.6-722437	13.140237	−72.410445	0.50	1.88 ± 0.20	0.29 ± 0.05	1.92 ± 0.26	2.39 ± 0.19	−0.43 ± 0.052	1.27 ± 0.13	10.6
J005504.3-722230	13.768110	−72.375004	0.89	1.94 ± 0.20	0.45 ± 0.06	1.32 ± 0.23	1.75 ± 0.10	−0.63 ± 0.035	1.15 ± 0.11	10.5

Notes. This table contains a subset of the catalog ranked by S/N and truncated at S/N > 10. The complete catalog in electronic form is available in the online version of this journal. Column definitions: R.A., decl.: coordinates incorporating the full *Chandra* aspect solution. $r95$: positional uncertainty for 95% confidence radius, F_{Bc}, F_{Sc},and F_{Hc}: energy flux in conventional broad, soft, and hard bands using source-appropriate spectral model based on quantiles. Quantiles: median photon energy (E50) and X,Y values for source in quantile parameter space (Hong et al. 2004). S/N: signal-to-noise ratio for broadband detection (net source counts divided by uncertainty).

(This table is available in its entirety in a machine-readable form in the online journal. A portion is shown here for guidance regarding its form and content.)

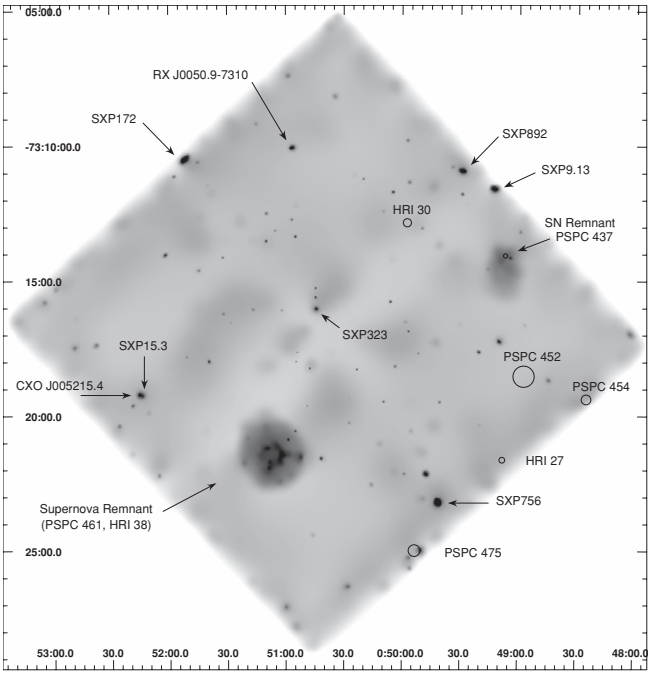

Figure 3. Adaptively smoothed broadband (0.3–8 keV) *Chandra* image of DF2, showing locations of pulsars, HMXB candidates, and unidentified *ROSAT* sources. The ACIS-I field measures $16' \times 16'$ on each side. Note the two SNRs: one is the brightest object in the image, the other is much fainter and located to the upper right. Pulsar SXP15.3 has a close (but resolved) neighbor which is itself a candidate HMXB. The many unidentified point sources are a mixture of quiescent XRBs (23 *Chandra* sources in this field have bright ($V < 17$) optical counterparts), stars, and background AGNs.

maximum scales for the smoothing kernel of 1–31 pixels). On these images, we overlay the detected HMXB candidates as well as previously known HMXBs.

3. TIMING ANALYSIS

Light curves were extracted in units of net count rate (i.e., background corrected counts per second) using good events from source and background regions of every sufficiently bright object detected. The light curves were extracted following the usual CIAO analysis thread with the tool *dmextract* at the intrinsic ACIS frame-time resolution of 3.2 s. Power density spectra (PDS) were computed using the Lomb–Scargle (LS) method (Scargle 1982) and all periods above 90% significance were flagged for further investigation. We analyzed both the complete light curves as well as the 2–3 individual segments per field listed in Table 1. The number of counts needed to unambiguously detect a pulse period depends on the ratio of period to observation duration, sampling interval, pulse fraction (PF), and pulse profile. Taking an optimistic cut at >100 net counts in 100 ks provides a lower threshold of approximately 10^{34} erg s^{-1} for detecting periodicities in SMC pulsars. The threshold for detecting a point source without regard to timing properties is about 10 times fainter. For comparison, the pulsation detection threshold (90%) for the *RXTE* SMC pulsar monitoring program is $\gtrsim 10^{36}$ erg s^{-1}, and only pulsed sources can be detected.

The periodogram analysis (Table 3) was conducted as a blind search (period search range 6–10,000 s) on every source with more than 50 net counts per light curve segment or 100 net counts for the stacked data. DF1 and DF2 contained 19 and 14 sources, respectively with >100 net counts. Spurious periods are expected near the *Chandra* dither periods (1000 s, 707 s), their harmonics (principally 500 s, 353 s), and the ACIS sampling period (3.2 s). Timing artifacts are only expected for sources that fall close to a CCD edge or node boundary. In this situation, the dither offsets can periodically move all or part of the source region on and off the detector, resulting in a modulation of the count rate. Examples of dither artifact can be seen in the PDS of several sources and are identified in the captions and/or accompanying the text. Significance levels for the periodograms were computed for all light curves according to the prescription of Press et al. (1992). A Monte Carlo approach was used to verify the significance levels in several cases noted in the discussion below. At each iteration, the flux values were randomly redistributed among the (unmodified) time bins and the periodogram computed. After 1000 iterations, we constructed the cumulative distribution of the maximum spectral power, in order to obtain the 95th percentile. This method accounts for the true distribution of flux values and the sampling pattern (e.g., gaps in the light curve).

In order to validate the results of the blind period search by the LS algorithm, we have also employed three other complimentary techniques: epoch folding (Leahy et al. 1984), Z^2 or Rayleigh statistic (Buccheri et al. 1983), and multi-Harmonic Periodogram (MHP; Schwarzenberg-Czerny 1996). For epoch folding, we accumulate both source and background photons in 10 phase bins at each trial period and calculate the χ^2-statistic of the background subtracted folded light curve with respect to the assumed constant rate. In our implementation of the Z^2-statistic, we calculate $n = 1$ harmonics (Z_1^2) using all the photons in the 95% point-spread function (PSF) of each source. While the epoch folding method is less dependent on the shape of the modulation profile, the Z_1^2 harmonic approach is relatively more sensitive to sinusoidal modulation. The latter takes advantage of the full timing resolution without resorting to binning but does not allow background subtraction, which is not a major concern since the background is relatively small and presumably non-periodic.

For each source with a positive period detection, the data were folded at the most probable period and grouped into 10 phase bins. Our folding code automatically establishes the epoch of peak flux by folding the data using the first data point as a trial epoch. The data are then folded a second time using the derived epoch, resulting in profiles with the peak flux ($p_{\max}$) at phase $\phi \sim 0$. This procedure greatly reduces systematic error caused by arbitrary choice of the number and placement of bins. Pulsed flux (f_p) and PF were computed from these pulse profiles according to the prescription of Bildsten et al. (1997). Our implementation is shown in Equations (1)–(3), where $\bar{f}$ is the mean flux and the phase interval $\phi = 0$–1 is typically divided into $n = 10$ equal width bins:

$$f_p = \int_0^1 [f(\phi) - f_{\min}] d\phi, \tag{1}$$

$$\simeq \frac{\sum_{i=1}^{n} (f_i - f_{\min})}{n}, \tag{2}$$

$$\mathrm{PF} = \frac{f_p}{\bar{f}}. \tag{3}$$

We note that f_p and hence PF are sensitive to errors on the minimum flux ($f_{\min}$), although this is always better constrained than $p_{\max}$. The phase-folded data points were also processed

Table 3
Pulsars Detected in the *Chandra* Data

Name	Source (CXOU)	Period (s)	Significance (%)	Net Counts	R.A. (deg)	Decl. (deg)	$r95\%(''$)
New pulsars in outburst							
SXP326	J005252.2-721715	326.79 ± 0.16	100.0	9292	13.217712	−72.287619	0.484
SXP892	J004929.7-731058	894.36 ± 0.98	100.0	1433	12.374103	−73.182874	0.485
Known pulsars detected with pulsations							
SXP138	J005323.8-722715	138.925 ± 0.028	...	1232	13.349580	−72.454325	0.296
SXP59	J005456.1-722648	58.8336 ± 0.0051	...	398	13.734005	−72.446703	0.504
SXP756	J004942.0-732314	746.24 ± 0.68	...	4116	12.425030	−73.387348	0.451
SXP323	J005044.6-731605	317.26 ± 0.12	...	2311	12.686208	−73.268118	0.289
SXP172	J005151.9-731033	171.851 ± 0.036	...	3322	12.966380	−73.176053	0.443
SXP8.88	J005153.3-723148	8.89909 ± 0.00008	...	184	12.972413	−72.530032	0.949
SXP15.3	J005214.0-731918	15.239 ± 0.01	...	147	13.058339	−73.321724	0.711
Known pulsars detected without pulsations							
SXP46.6	J005355.3-722645	...	...	63	13.480710	−72.4460110	0.366
SXP7.78	J005205.6-722604	...	...	76	13.023633	−72.4344790	0.769
SXP9.13	J004913.5-731138	...	...	1178	12.306384	−73.1939050	0.527
SXP342	J005403.9-722633	...	...	36	13.516329	−72.4425030	0.428
Known pulsars in the field not detected							
SXP4.78							
SXP82.4							
Other periodic candidates							
	J005446.3-722523	4693 ± 20	99.0	140	13.693000	−72.423111	0.562
	J005331.7-722240	131.114 ± 0.02	91.5	386	13.382157	−72.378046	0.373
	J005437.1-722637	10.4258 ± 0.01	90.4	433	13.654878	−72.443838	0.415

Notes. $r95$ is the radius of the 95% statistical confidence region on the source position. It does not include the $0''.75$ systematic aspect uncertainty. Significance is computed for a blind search in period range 6.5–10,000 s, it is not quoted for pulsars with known periods.

with the *loess* algorithm, a nonparametric smoother (Cleveland 1981) to obtain an unbinned visualization of the pulse profile. A best-fitting sine wave is also overplotted.

Several of the *Chandra* sources were firmly identified as known HMXB pulsars by their coordinates. In these cases, the pulse period is well known and it is not appropriate to use a blind-search approach to period detection. Instead a narrower period range centered on the known pulse period must be examined; following the approach used in the *RXTE* pulsar monitoring pipeline (L05) we chose 5% either side of the literature period. If a periodogram peak is detected at a period consistent with the historical record for that particular pulsar it constitutes a valid measurement of the pulsar. For this purpose, we examined the decade-long *RXTE* pulse-period history of Galache et al. (2008). In cases where no significant peak is found, the maximum periodogram value in the expected period range may be interpreted as an upper limit on the pulsed flux.

At our detection limit of 4×10^{32} erg s^{-1} (five net counts at the ACIS-I aim point in 100 ks, assuming $D_{\rm SMC} = 60$ kpc, $\Gamma = 1$, $N_{\rm H} = 5 \times 10^{21}$ cm^{-2}), we expect to detect the high luminosity end of the SMC populations of flaring stellar coronae and CVs. CVs (accreting white dwarfs) and LMXBs (accreting NS and black hole binaries) exhibit aperiodic variability (flickering) over a wide range of timescales from milliseconds up. Such variability produces a characteristic power-law distribution (red noise) in the PDS which can be spotted by visual inspection. No such features were detected in the bright sources selected for timing analysis. To search for other variability, light curves binned by 16 times the ACIS frame time were visually inspected for all sources with at least 50 counts in the stacked data set. This search turned up a foreground flare star (CXOU J005428.9-723107) in DF1 which is the subject of a separate analysis by Laycock & Drake (2009). None of the other 95 sources so examined showed any outstanding feature in their light curve.

4. SPECTRAL ANALYSIS

X-ray spectral analysis requires a reasonable number of photons and was performed for the 14 sources with more than 250 net counts in the stacked data set. Spectra were extracted from the ChaMP pipeline source and background event files using CIAO 3.4 and grouped to give 10 source counts per spectral bin. Spectral fits were performed with XSPEC, the results of which are given in Table 4. Eight of these sources are pulsars and are well described by the power-law $\Gamma \sim 1$ model typical of X-ray pulsars over this energy range. Photon indices are in the range 0.7–1.3, and derived neutral hydrogen column densities lie in the range (0.6–10) $\times$ 10^{21} cm^{-2}. Two probable HMXBs (CXO J5057.1-731008 = RX J0050.9-7310 and CXO J005215.4-731915) also exhibit $\Gamma \sim 1$ X-ray spectra; neither has been definitively identified with pulsations. Three of the remaining spectra are softer, showing $\Gamma \sim 1.8$, suggestive of AGNs. This picture is muddied by the detection of candidate periodicities in the X-ray light curves of two of them (Table 3), although these could be spurious and due to aperiodic noise. Finally, the softest spectrum belongs to a foreground flare star. Pileup (multiple photons contributing to a single ACIS charge island during the 3.2 s readout period) can be safely ignored for all our sources, the brightest of which has a count rate of 0.10 counts s^{-1}, which would result in only a few percent pileup.

The majority of the sources in our catalog are too faint for spectral fitting, and we therefore turn to quantile analysis (Hong et al. 2004). Quantile analysis is a method to optimally extract spectral information from low count X-ray sources, without

Table 4
Spectral Fits (Sources with >250 Net Counts)

CXOU	$n_{\rm H}$ (10^{21} cm^{-2})	Γ	Spectrum Bins	χ^2_ν	f_X (2–10 keV) ($\times 10^{-13}$ erg cm^{-2} s^{-1})	Remarks
J004913.5-731138	10.13 ± 1.33	1.34 ± 0.12	67	1.27	4.635	SXP9.13
J004929.7-731058	7.69 ± 1.01	0.96 ± 0.10	81	0.96	6.958	SXP892
J004942.0-732314	5.95 ± 0.49	1.04 ± 0.05	197	0.98	17.97	SXP756
J004948.2-732211	4.95 ± 2.14	1.73 ± 0.24	27	1.46	1.111	AGN (1)
J005044.6-731605	3.49 ± 0.59	0.89 ± 0.07	123	0.98	10.33	SXP323
J005057.1-731008	5.20 ± 1.48	1.07 ± 0.1	42	0.86	3.012	RX J0050.9
J005151.9-731033	1.58 ± 0.29	1.14 ± 0.05	159	1.02	10.24	SXP172
J005215.4-731915	0.65 ± 1.50	0.93 ± 0.20	20	1.21	1.133	HMXB? (2)
J005252.2-721715	3.44 ± 0.23	1.14 ± 0.03	322	1.25	29.34	SXP326
J005323.8-722715	2.30 ± 0.77	0.76 ± 0.09	71	0.77	5.241	SXP138
J005331.7-722240	2.39 ± 1.52	1.84 ± 0.22	23	1.34	0.629	(3)
J005428.9-723106	1.65 ± 0.94	2.91 ± 0.30	17	0.24	0.149	Flare star (4)
J005437.1-722637	1.57 ± 1.25	1.81 ± 0.21	26	1.4	0.667	(3)
J005456.1-722648	1.69 ± 1.54	0.90 ± 0.21	24	1.39	1.369	SXP59

Notes. (1) AGN based on spectral fit, lack of counterpart, or periodicity. (2) HMXB based on spectrum, optical, and *XMM-Newton* (Haberl et al. 2008) counterpart, see Section 5.12. (3) AGN-like spectrum, no counterpart, candidate period, see Table 3. (4) Laycock & Drake (2009).

imposing arbitrary energy-band choices. The advantage over X-ray color indices is that all sources can be represented in the same parameter space, with a somewhat uniform error distribution. Energy-band choices made in generating hardness ratios and color indices inevitably lead to some sources having a gross imbalance in the number of counts in each band. Following the methods of Hong et al. (2005), background corrected quantile values (QDx and QDy) were computed from each source's event list photon energy distribution, and spectral model grids were generated using the full *Chandra* ACIS-I response function (ARF and RMF). The quantile values, along with overplotted model grids for absorbed power law and thermal bremsstrahlung (TB), are plotted in Figure 20 for a series of cuts in signal-to-noise ratio (S/N > 3, >5, >10). These figures may be used in interpreting the quantile values presented for the DF source catalog (Table 2).

X-ray luminosity is computed throughout the paper using $D_{\rm SMC} = 60$ kpc (Hilditch et al. 2005).

5. HIGH-MASS X-RAY BINARIES AND CANDIDATES

In order to identify HMXBs, make associations with previously unclassified sources, and assess evidence of historical variability for new candidate systems, we compared our *Chandra* DF source list against a number of published X-ray source catalogs and works on SMC HMXBs. The results of this analysis are presented below in the form of a source by source (in R.A. order) discussion of all HMXBs and candidates that were observed in our *Chandra* program. An additional group of sources with bright HMXB-like optical counterparts is summarized in Section 6; these objects lack conclusive timing and spectral information and are not associated with literature X-ray sources.

Prior to our *Chandra* observations, there were 12 known X-ray pulsars covered by these observations: seven in Field-1 and five in Field-2. We saw strong pulsations in five of the known pulsars (SXP756, SXP326, SXP172, SXP138, and SXP59) and weak pulsations in two others (SXP8.88 and SXP15.3). Three known pulsars (SXP9.13, SXP7.78, and SXP46.6) were detected as point sources but without pulsations being discernible, and two known pulsars were not detected: SXP82.4 and SXP4.78.

Table 5
Orbital Phase of Known Pulsars During *Chandra* Observations

Name	Field	Mid-time MJD	Period (days)	Epoch MJD	Phase (ϕ)
SXP138[a]	1	53851	103.6	52400.5	0.001
SXP59[a]	1	53851	122.10	52306.1	0.653
SXP756[a]	2	54061	389.9	52196.1	0.783
SXP323[a]	2	54061	116.6	52336.9	0.786
SXP172[a]	2	54061	...	...	...
SXP8.88[a]	1	53851	28.47	52392.2	0.240
SXP46.6[b]	1	53851	137.36	52293.9	0.336
SXP15.3[a]	2	54061	...	...	...
SXP7.78[b]	1	53851	44.92	52250.9	0.621
SXP9.13[b]	2	54061	77.2	52380.5	0.768
SXP4.78[c]	1	53851	...	...	...
SXP82.4[c]	1	53851	362.3	52089.0	0.863

Notes. Phases computed according to the ephemerides of the *RXTE* monitoring project (Galache et al. 2008). The phase convention places the X-ray outburst peak at $\phi = 0.5$, which is presumed to reflect the time of periastron.
[a] Pulsations identified.
[b] Point source without pulsations.
[c] Not detected.

The position plotted for the undetected pulsar SXP4.78 in Figure 2 is that of the proposed optical counterpart, the emission-line star [MA93]537. The *RXTE* position for SXP4.78 (Laycock et al. 2003) is subject to a $\sim 1'$ uncertainty which lies wholly within (but close to the edge of) DF1. We can therefore say that no 4.78 s pulsar was detected in the error box of SXP4.78. Subject to the optical counterpart being correct, the *Chandra* non-detection places an upper limit of $L_X < 1.1 \times 10^{33}$ erg s^{-1} (equivalent to 10 net counts at the position of [MA93]537, scaled by the normalized exposure map value 0.83).

Most of the known Be/XRBs in the SMC are seen regularly by the *RXTE* monitoring program (L05; G08) and as a result have known X-ray ephemerides. We calculated the orbital phase for each detected pulsar in order to search for quiescent emission in systems far from periastron; this phase information is given in Table 5. As a caveat, we remind the reader that X-ray ephemerides are based on the spacing of X-ray outbursts and thus may not exactly reflect the orbital parameters; for example, there might be shifts between outburst peak and periastron.

Table 6
ROSAT HRI Counterparts from Sasaki et al. (2000) Catalog

CXOU	SXP	r_{CXO} ($''$)	PSPC	HRI	r_{HRI} ($''$)	Sep ($''$)	r_{Total} ($''$)	Remarks
J005057.1-731008		0.46	421	36	3.3	2.21	3.33	HMXB, AX J0050.8-7310
J005209.2-722553		1.59	...	43	15.9	7.53	15.98	HRI:SMC X-3 $\neq$ CXO
J005214.0-731918	SXP15.3	0.71	453	44	1.1	0.46	1.31	RX J0052.1-7319

Table 7
ROSAT PSPC Counterparts from Haberl et al. (2000) Catalog

CXOU	SXP	r_{CXO} ($''$)	PSPC	r_{PSPC} ($''$)	Sep ($''$)	r_{Total} ($''$)	Remarks
J004824.0-731918		4.14	454	10.8	5.70	11.57	RX J0048.4-7319, SNR 0046-73.5
J004913.5-731138		0.53	430	6.1	4.73	6.12	RX J0049.2-7311, SXP9.13?
J004929.7-731058	SXP892	0.49	427	5.5	2.82	5.52	RX J0049.5-7310
J005057.1-731008		0.46	421	4.5	2.45	4.52	RX J0050.9-7310, AX J0050.8-7310
J005153.2-723148	SXP8.89	0.95	265	45.8	20.31	45.81	RX J0051.8-7231
J005352.5-722639		0.51	242	25.7	21.52	25.71	Be, HMXB?
J005354.8-722722		0.47	242	25.7	22.78	25.70	AGN?
J005355.3-722645	SXP46.6	0.37	242	25.7	17.57	25.70	RX J0053.9-7227, XTE J0053-724
J005428.8-722810		1.96	248	45.7	19.76	45.74	RX J0054.5-7228
J005433.0-722806		1.83	248	45.7	1.23	45.74	RX J0054.5-7228
J005436.5-722816		2.29	248	45.7	17.63	45.76	RX J0054.5-7228

Note. See the text for discussion of multiple associations.

The *RXTE* light curves themselves provide additional context because they record the general state of activity (and pulse period) in each pulsar around the times of the DF1 and DF2 observations.

We refer to the SMC X-ray Pulsar (SXP) compilation for *RXTE* monitoring results (Galache et al. 2008), the *ROSAT* source catalogs of Haberl et al. (2000) and Sasaki et al. (2000) (for the PSPC and HRI instruments, respectively), and the catalog of Yokogawa et al. (2003, hereafter Y03) for *ASCA* results. Published observations with *XMM-Newton* of HMXBs in the SMC Bar were also consulted, principally Haberl et al. (2008) which became available while the present work was in progress.

Possible *ROSAT* counterparts were identified by combining the *Chandra* and *ROSAT* error radii in quadrature. The Y03 *ASCA* catalog does not provide positional error estimates, so we relied instead on their tabulated cross identifications with HRI sources. The complete Y03 catalog contains 38 *ASCA* sources with HRI counterparts. Examination of the distribution of the separations (column "Sep2" in Y03) for these objects shows that 95% lie within Sep2 <= 52$''$, which we adopted as our search radius.

Eleven *Chandra* sources match seven PSPC sources (two of the PSPC sources have three *Chandra* matches each). Three *Chandra* sources have (unique) HRI counterparts. Forty-four *Chandra* sources match 13 *ASCA* sources (multiple matches due to the relatively large positional uncertainties). In many cases, the multiple matches can be resolved by the detection of pulsations or by YO3's identifications with *ROSAT* sources. The 10 confirmed HMXBs are separated into Part 1 of the table, the remainder (Part 2) are a combination of chance positional matches and partially resolved SNRs.

We searched for optical counterparts consistent with HMXBs using the emission-line star catalog of Meysonnier & Azzopardi (1993, hereafter MA93), and the Magellanic Clouds Photometric Catalog (hereafter MCPS) of Zaritsky et al. (2002). In the case of the literature X-ray sources, most of these counterparts have been previously reported, unless otherwise stated in the discussion.

The results of our literature search appear in Table 3 for the SXP pulsars and Tables 6–9 for HRI, PSPC, *ASCA*, and *XMM-Newton* catalogs, respectively. Optical emission-line counterparts are given in Table 10 and MCPS stars in Table 11. For completeness, we list all matches, resulting in some objects appearing more than once in the tables. All such duplications are disambiguated in the source-by-source discussion that follows.

In summary, we detected 13 of the 15 pulsars now known in the fields, including 2 new pulsars and 5 additional HMXB candidates based on timing, spectra, and association with existing X-ray and optical catalogs. Using the MA93 and MCPS catalogs, we identified a total of 40 *Chandra* sources with bright ($V < 17$) optical counterparts, of which ~half are confirmed HMXBs and all but 6 of the remainder are considered candidates (see Section 6).

5.1. CXOU J004913.5-731138–SXP9.13

We detected both of the two *ROSAT* sources (see Table 7) that have been proposed by Filipovic et al. (2000) as candidates of the *ASCA* pulsar AX J0049-732 = SXP9.13. The source preferred by Filipovic et al. (2000; No. 427, RX J0049.5-7310 = CXOU J004929.7-731058) as being the *ASCA* pulsar based on a positionally coincident emission-line star (MA93 No. 300) is found by us to be a $P = 892$ s pulsar (see Figure 4 and Table 3). Both X-ray sources were detected by Haberl & Pietsch (2004) in *XMM-Newton* observations from 2000 October, at which time pulsations were not detected in either source. The discovery of SXP892 appears to partially resolve the ambiguous identity of AX J0049-732 as there is now only one candidate (No. 430 RX J0049.2-7311 = CXOU J004913.5-731138). The possibility remains that the *ASCA* pulsar is not this object and the case will be fully resolved only if the *Chandra* source shows 9.13 s pulsations. CXOU J004913.5-731138 was relatively bright (1178 net ACIS counts); however, pulsations were not detected, despite the time resolution of *Chandra* ACIS (3.2 s) being sufficient to critically sample the 9.13 s pulse period. The periodogram (Figure 5) evaluated over a period range covering $P = 9.13$ s $\pm$ 5% contains many noise peaks of similar height,

Table 8
ASCA Counterparts from Yokogawa et al. (2003) Catalog

CXOU	*ASCA*	Sep (″)	PSPC	HRI	Remarks
Part 1: Identified HMXBs					
J004913.5-731138	26	31.5	430	...	AX J0049-732, RX J0049.0-7314 [SXP9.13?]
J004929.7-731058	27	16.8	427	...	RX J0049.4-7310 [SXP892]
J004942.0-732314	30	34.5	468	...	AX J0049.5-7323, RX J0049.7-7323 [SXP756]
J005044.6-731605	32	26.3	444	34	AX J0051-733, RX J0050.8-7316 [SXP323]
J005057.1-731008	35	15.7	421	36	RX J0050.9-7310 [HMXB]
J005151.9-731033	40	32.2	424	41	AX J0051.6-7311 [SXP172]
J005214.0-731918	43	37.2	453	44	RX J0052.1-7319 [SXP15.3]
J005355.3-722645	47	3.7	242	51	1WGA J0053.8-7226 [SXP46]
J005403.9-722633	47	40.4	242	51	1WGA J0053.8-7226 [SXP342]
J005456.1-722504	51	51.4	241	58	XTE J0055-724, 1SAX J0054.9-7226 [SXP59]
Part 2: Positional matches without positive identification					
J004845.4-731842	23	37.5	454	...	SNR 0046-735
J0049-0.0-731314	25	36.5	437	...	SNR 0047-735
J004927.1-731211	26	39.1	430	...	AX J0049-732
J004929.8-731150	26	50.3	430	...	AX J0049-732
J004934.7-731049	27	36.6	427	...	RX J0049.4-7310
J004937.4-732228	30	25.6	468	...	AX J0049.5-7323
J004948.2-732211	30	37.1	468	...	AX J0049.5-7323
J005037.2-731530	32	20.9	444	34	AX J0051-733
J005044.8-731618	32	37.2	444	34	AX J0051-733
J005045.0-731539	32	20.6	444	34	AX J0051-733
J005045.0-731519	32	33.0	444	34	AX J0051-733
J005047.6-731619	32	45.2	444	34	AX J0051-733
J005047.8-731736	34	23.7		...	
J005048.7-732115	36	45.3	461	38	SNR 0049-736
J005049.6-730926	35	44.1	421	36	RX J0050.9-7310
J005049.7-731608	32	45.9	444	34	AX J0051-733
J005052.4-732135	36	47.2	461	38	SNR 0049-736
J005054.3-731741	34	30.2		...	
J005054.5-731027	35	21.1	421	36	RX J0050.9-7310
J005055.0-731802	34	50.1		...	
J005055.4-732036	36	21.6	461	38	SNR 0049-736
J005059.0-732055	36	4.2	461	38	SNR 0049-736
J005102.9-732126	36	37.7	461	38	SNR 0049-736
J005103.4-732139	36	49.6	461	38	SNR 0049-736
J005104.4-732108	36	30.5	461	38	SNR 0049-736
J005145.1-731038	40	5.2	424	41	AX J0051.6-7311
J005215.4-731915	43	30.2	453	44	RX J0052.1-7319
J005218.9-731940	43	37.3	453	44	RX J0052.1-7319
J005225.9-731921	43	22.7	453	44	RX J0052.1-7319
J005352.5-722639	47	12.3	242	51	1WGA J0053.8-7226
J005354.8-722722	47	40.5	242	51	1WGA J0053.8-7226
J005357.6-722605	47	38.4	242	51	1WGA J0053.8-7226
J005358.5-722614	47	31.0	242	51	1WGA J0053.8-7226
J005406.0-722650	47	49.7	242	51	1WGA J0053.8-7226

Notes. *Chandra* and *ASCA* coordinates were matched using a 52″ search radius, determined from the 95th percentile of the distribution of separations between *ASCA* and *ROSAT* HRI coordinates in the complete *ASCA* catalog of the SMC (Yokogawa et al. 2003). Many of the *ASCA* sources have multiple *Chandra* positional coincidences, those which are not definitely identified with specific HMXBs are listed in Part 2 of the table. The PSPC, HRI, and Remarks columns are drawn directly from the Yokogawa et al. (2003) catalog, modified in the case of Part 1, with the SXP designation added if known. The PSPC and HRI source numbers derive from Haberl et al. (2000) and Sasaki et al. (2000) and can be compared with Tables 7 and 6.

and the PF must therefore be very small at this time. The orbital phase (G08 ephemeris, Table 5) was 0.82, outside the range of the normal outbursts seen in SXP9.13, and therefore presumably far from periastron, which can account for the lack of pulsations. We measured a luminosity of $L_x = 8.5 \times 10^{34}$ erg s^{-1} (B_C band). This source was again detected by *XMM-Newton* on 2007 March 12 by Haberl et al. (2008); the *XMM-Newton* and *Chandra* coordinates are separated by 1.″29 within an error budget of 2.″01 (quadrature sum of 95% statistical and systematic errors for both telescopes).

5.2. CXOU J004824.0-731918

This source lies 5.″7 away from *ROSAT* source RX J0048.4-7319 (PSPC No. 454, see Table 7). The *ROSAT* object was associated with the supernova remnant SNR 0046-73.5 by Haberl et al. (2000) and is indicated on the *Chandra* DF2 image

Table 9
XMM-Newton Counterparts from Haberl et al. (2008)

CXOU	r_{CXO} (″)	$r_{XMM\text{-}Newton}$ (″)	r_{Total} (″)	Sep (″)	Remarks
J004913.5-731138	0.53	0.55	2.01	1.29	RX J0049.2-7311, SXP9.13
J004929.7-731058	0.49	0.81	2.09	1.04	RX J0049.5-7310, SXP892
J004942.0-732314	0.45	0.23	1.93	0.07	RX J0049.7-7323, SXP755
J005044.6-731605	0.29	0.18	1.89	0.13	RX J0050.8-7316, SXP323
J005151.9-731033	0.44	0.59	2.00	1.19	AX J0051.6-7311, SXP172
J005215.4-731915	0.61	0.82	2.12	1.21	Close to SXP15.3 (Section 5.12)
J005205.6-722604	0.77	0.14	2.02	1.17	SMCX-3, SXP7.78
J005252.2-721715	0.48	0.21	1.93	0.66	XMMU J005252.1-721715, SXP326
J005323.8-722715	0.30	0.16	1.89	0.42	CXOU J005323.8-722715, SXP138
J005403.9-722633	0.43	0.27	1.93	0.27	XMMU J005403.8-722632, SXP342
J005456.1-722648	0.50	0.36	1.96	1.05	XTE J0055-724, SXP59

Table 10
Emission-line Star Counterparts in MA93 Catalog

CXOU	MA93	Sep (″)	r_{CXO} (″)	r_{Total} (″)	Remarks
J004849.0-731625	258	2.29	4.30	5.0	Be?
J004929.7-731058	300	0.62	0.49	2.7	SXP892
J004942.0-732314	315	1.05	0.45	2.6	SXP756
J005012.2-731156	341	0.77	1.51	3.0	Be?
J005036.0-731739	374	0.28	0.48	2.7	Be?
J005044.6-731605	387	0.59	0.29	2.6	SXP323
J005057.1-731008	414	0.87	0.46	2.7	Be?, RX J0050.9-7310
J005117.0-731606	448	0.59	0.63	2.7	Be?
J005151.9-731033	504	1.10	0.44	2.6	SXP172
J005153.2-723148	506	0.20	0.95	2.8	SXP8.89
J005205.6-722604	531	1.37	0.77	2.7	SMC X-3
J005214.0-731918	552	0.65	0.71	2.7	SXP15.3
J005237.3-722732	590	1.09	0.93	2.8	Be?
J005323.8-722715	667	0.97	0.29	2.6	SXP138
J005329.2-723348	677	1.40	2.60	3.7	Be?
J005352.5-722639	717	0.84	0.51	2.7	Be(1)
J005446.3-722423	798	2.56	0.56	2.7	Be?
J005456.1-722648	810	1.45	0.50	2.7	SXP59

Notes. The matching radius r_{Total} is the quadrature sum of r_{CXO}, 0.″75 aspect uncertainty and 2.″5 tolerance on the MA93 coordinates. New X-ray plus emission-line counterparts are indicated by "Be?" in the Remarks column. (1) Confirmed Be star, see Section 5.16.

(Figure 3). The object is at outer edge of the *Chandra* ACIS-I array at an off-axis distance of ∼8 arcmin. Consequently, the object could be either a bright region of the SNR or point source, the lack of a bright-star counterpart rules out an HMXB and favors the former explanation.

5.3. CXOU J004929.7-731058–SXP892

This source is detected in DF2 with 1434 net counts. This is a new pulsar with an 894 s period. The pulsation is detected at very high significance as shown in Figure 6. The derived luminosity is $L_x = 9.3 \times 10^{34}$ erg s^{-1}, consistent with a faint type I (normal) outburst from a Be XRB pulsar. The ACIS spectrum from 0.35–8 keV is well fit by a power law with photon index $\Gamma = 1$ and very low extinction (Table 4). DF2 was observed by *Chandra* in 2002 for 10 ks, when SXP892 was not detected, confirming its transient nature. Had it been active at the same level it would have registered ∼143 counts. The fact that SXP892 has never been detected above the pulsed flux limit of *RXTE* (∼10^{36} erg s^{-1}), despite being frequently in the field of view indicates that its outbursts are always faint. The position of SXP892 coincides with the *ROSAT* and *XMM-Newton* source RX J0049.5-7310 (Haberl & Pietsch 2004), as shown in Table 7 and Figure 4. The separation between the *Chandra* and HRI coordinates is 2.″82 with a total error budget of 5.″52. An emission-line star (No. 300 in MA93) was associated with RX J0049.5-7310 by Filipovic et al. (2000). The star is also coincident with our *Chandra* position (Table 10) and is in the MCPS catalog with $V = 16.15$ mag, $B - V = 0.20$ mag (see Table 11). The discovery of an outburst and 892 s pulse period confirms the object as a Be-HMXB pulsar.

5.4. CXOU J004942.0-732314–SXP756

We detected SXP756 (Yokogawa et al. 2000) with 4116 counts in DF2. Figure 7 shows the power spectrum and folded pulse profile, which exhibits one prominent narrow peak per cycle defined as $\phi = 0$, plus a much smaller (and possibly broader) peak at $\phi = 0.5$. The pulse period was 746 s which is at the shorter end of the period range (746–767 s) seen by G08 with *RXTE*. The X-ray spectrum is well described by an absorbed power law ($\Gamma = 1.0$, $n_H = 5 \times 10^{21}$ cm^{-2}) with luminosity $L_X = 7.7 \times 10^{35}$ erg s^{-1}. According to the G08 ephemeris (Table 5), the orbital phase of the system was 0.78 in the quiescent portion of the long-term *RXTE* light curve. The pulsed flux from the *RXTE* data folded at the orbital period of 389.9 days shows that in addition to regular outbursts, activity at $L_X \sim 10^{36}$ erg s^{-1} has occurred sporadically throughout most of the cycle. This persistent pulsed emission is confirmed by the *Chandra* results, which show a low pulsed fraction (∼25%).

5.5. CXOU J005044.6-731605–SXP323

We detected a bright source with pulse period 317.3 s (Figure 8), located at the coordinates of SXP323 which is likely the same pulsar, although the period differs significantly from the discovery value of 323 s (Yokogawa et al. 2003). The *RXTE* monitoring program detected the system in outburst on MJD 52960 with pulse period 317 s (100% period-detection significance, uncertainty <0.1 s), following an erratic multi-year trend of decreasing period (spin-up). Galache et al. (2008) attributed the MJD 52960 outburst to a type II (super-outburst) event as it did not follow the ephemeris derived from previous and subsequent outbursts. At the time of the DF2 observation (MJD 54061), the orbital phase of SXP323 was 0.8 (G08 ephemeris, Table 5) and the pulsar was far from its presumed periastron. During the ∼3 yr between the super-outburst and our *Chandra* observation, the pulsar has not slowed, but has rather continued the gradual spin-up trend. Haberl et al. (2008) demonstrate that *ASCA* and *XMM-Newton* data confirm long-term spin-up of SXP323 and point out that *RXTE*'s turbulent period history could

Table 11
Optical Counterparts $V < 17$ in MCPS Catalog

CXOU	r_{CXO} ($''$)	Sep ($''$)	r_{Total} ($''$)	Net Counts	R.A.	Decl.	Vmag	$B-V$	ID
J004849.0-731625	4.31	1.84	4.37	9.0	12.2057	−73.27337	14.56	−0.06	[MA93]258
J004913.5-731138	0.53	0.83	0.92	1178.2	12.3070	−73.19376	16.44	0.19	SXP9.13
J004922.2-732006	3.31	1.86	3.40	7.2	12.3409	−73.33498	16.62	0.09	C
J004929.7-731058	0.48	0.43	0.89	1433.9	12.3745	−73.18284	16.15	0.20	SXP892
J004941.3-731353	1.40	0.94	1.59	9.8	12.4215	−73.23132	15.84	1.89	R
J004942.0-732314	0.45	0.08	0.88	4116.9	12.4251	−73.38734	14.86	0.15	SXP755
J004958.8-731634	0.97	0.43	1.23	5.8	12.4955	−73.27627	14.53	0.57	R
J005002.4-731210	1.66	0.61	1.82	7.7	12.5104	−73.20317	15.74	0.94	R
J005004.4-731426	1.41	0.44	1.59	3.7	12.5187	−73.24079	15.50	0.06	C
J005012.2-731156	1.51	1.07	1.69	8.2	12.5520	−73.19892	15.31	0.16	[MA93]341
J005035.5-731401	0.86	0.64	1.14	4.7	12.6485	−73.23401	15.99	0.11	C
J005036.0-731739	0.48	0.35	0.89	10.2	12.6506	−73.29428	15.61	0.08	[MA93]374
J005044.6-731605	0.29	0.31	0.80	2311.8	12.6865	−73.26814	15.48	−0.11	SXP323
J005047.8-731736	0.62	0.25	0.97	4.8	12.6994	−73.29346	16.58	0.01	C
J005047.9-731817	0.39	0.26	0.85	41.9	12.7001	−73.30496	15.07	0.12	C
J005057.1-731008	0.46	0.37	0.88	700.1	12.7382	−73.16883	14.35	0.08	[MA93]414 PSPC
J005105.7-731312	0.96	0.77	1.22	7.7	12.7741	−73.21983	15.70	0.07	C
J005117.0-731606	0.63	0.81	0.98	9.3	12.8217	−73.26843	15.00	0.18	[MA93]448
J005151.9-731033	0.44	0.65	0.87	3322.7	12.9670	−73.17608	14.45	−0.07	SXP172
J005153.2-723148	0.95	0.52	1.21	183.9	12.9716	−72.53010	14.38	0.41	SXP8.88
J005205.6-722604	0.77	0.19	1.07	76.0	13.0237	−72.43443	14.91	−0.00	SMC X-3
J005207.5-722126	1.88	1.40	2.03	26.4	13.0312	−72.35704	15.20	−0.07	C
J005214.0-731918	0.71	0.44	1.03	146.9	13.0587	−73.32179	14.49	0.14	SXP15.3
J005215.4-731915	0.61	0.37	0.97	286.7	13.0645	−73.32086	15.90	−0.14	C
J005230.6-731532	5.26	4.29	5.31	6.2	13.1313	−73.25964	16.22	1.00	R
J005237.3-722732	0.93	0.48	1.19	12.0	13.1556	−72.45897	14.98	0.01	[MA93]590
J005245.1-722844	0.91	0.98	1.18	12.0	13.1879	−72.47871	14.92	0.00	C
J005251.4-731451	6.52	3.95	6.57	8.7	13.2180	−73.24753	15.85	0.87	R
J005252.2-721715	0.48	0.72	0.89	9292.4	13.2177	−72.28742	16.62	−0.20	SXP326
J005314.6-721848	1.83	1.77	1.98	24.0	13.3117	−72.31398	16.39	0.61	R
J005323.8-722715	0.30	0.17	0.81	1232.0	13.3496	−72.45428	16.19	−0.09	SXP138
J005329.2-723348	2.60	1.00	2.71	11.5	13.3724	−72.56333	14.62	0.01	[MA93]677
J005331.8-721845	5.09	4.78	5.15	6.4	13.3806	−72.31389	16.03	−0.17	C
J005349.0-722506	0.50	0.32	0.90	13.2	13.4544	−72.41837	16.62	1.07	R
J005355.3-722645	0.37	0.38	0.83	62.9	13.4808	−72.44591	14.72	−0.07	SXP46.6
J005403.9-722633	0.43	0.23	0.86	36.3	13.5163	−72.44244	14.94	0.01	SXP342
J005419.2-722049	5.78	1.92	5.83	3.6	13.5787	−72.34728	16.97	−0.05	C
J005446.3-722523	0.56	0.55	0.94	140.4	13.6933	−72.42298	15.36	0.14	[MA93]798, $P = 4693$
J005456.1-722648	0.50	0.88	0.90	398.9	13.7344	−72.44649	15.27	−0.05	SXP59
J005507.7-722241	0.94	0.57	1.20	114.9	13.7827	−72.37801	14.38	−0.13	C

Notes. The matching radius r_{Total} is the quadrature sum of r_{CXO} and $0''.75$ aspect uncertainty. The ID column shows confirmed HMXBs, objects identified with MA93 stars in Table 10, and the codes C = "blue early-type candidate" and R = "red-outlier" based on the $B-V$ color index compared to the confirmed HMXBs.

be contaminated by frequencies arising from nearby SXP326 (Section 5.13).

5.6. CXOU J005057.1-731008–RX J0050.9-7310

A *ROSAT* source consistent with CXOU J005057.1-731008 (Figure 3) appears in the HRI (No. 36) and PSPC (No. 421) catalogs at very small positional offsets. Both source coordinates agree at the $\sim 2''$ level, within a total error budget of $\sim 4''$. There is also an *ASCA* counterpart (Table 8, No. 35 in Yokogawa et al. 2003), identified with the same *ROSAT* source (AX J0050.8-7310 = RX J0050.9-7310), an association backed up by *XMM-Newton* results (Haberl & Pietsch 2004; Shtykovskiy & Gilfanov 2005).

Haberl & Sasaki (2000) proposed this source to be a Be-XRB, based on its association with an emission-line star (No. 414 in MA93), which is confirmed by our *Chandra* error circle (Table 10). The star also appears in MCPS with $V = 14.35$ mag, $B - V = 0.08$ mag. The *Chandra* ACIS spectrum in the DF2 data set is well fit (reduced $\chi^2 = 0.86$) by an absorbed power law with photon index $\Gamma = 1.07 \pm 0.1$ and absorption column density $n_H = (5.20 \pm 1.48) \times 10^{21}$ cm^{-2} which is typical for HMXB pulsars in the SMC. The source shows strong variability between the *ROSAT*, *ASCA*, and the 2006 *Chandra* observations. Together, these lines of evidence strongly support the Be-XRB classification, although pulsations have not been detected.

5.7. CXOU J005151.9-731033–SXP172

SXP172 was detected with pulse period 171.8 s (Figure 9) in DF2 (MJD 54061) with 2–10 keV luminosity $L_x = 1.53 \times 10^{35}$ erg s^{-1}. The pulsar has historically shown a prolonged episode (MJD 51500-52500) of steady spin-up (see G08, Figure 30). The period detected here is in line with the end of that active episode, indicating that the pulsar has not continued to spin up during the $\sim$1000 days since its activity dropped

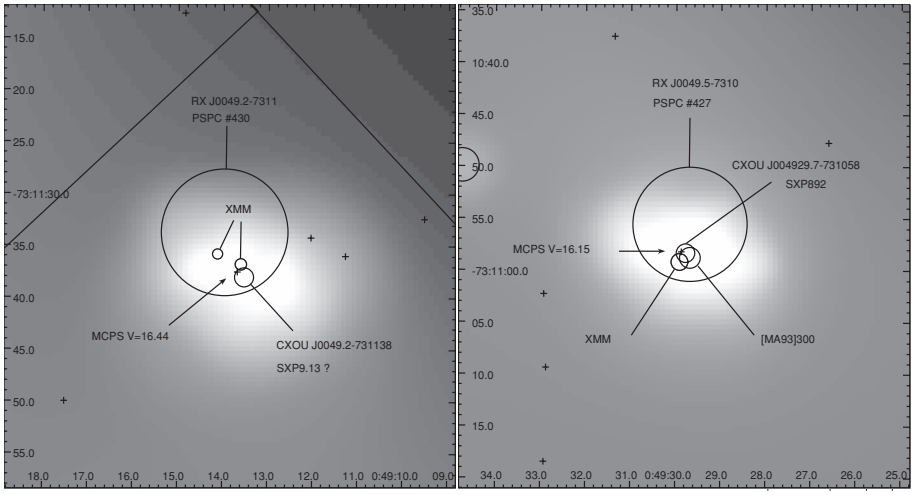

Figure 4. *Chandra* ACIS images of the neighboring bright X-ray sources CXOU J0049.2-731138 = RX J0049.2-7311 (left) and CXOU J004929.7-731058 = RX J0049.5-7310 (right). Both sources lie inside the *ASCA* error circle for the pulsar SXP9.13 (Filipovic et al. 2000). We find that CXOU J004929.7-731058 is a new 892 s pulsar, thus RX J0049.2-7311 is probably SXP9.13, although some ambiguity remains as the 9.13 s pulsations have not been localized to sufficient precision. Labeled circles indicate positional error radii for *Chandra*, *ROSAT,* and *XMM-Newton* (Haberl et al. 2008) detections. Bright stars ($V < 17$) in the MCPS catalog are indicated by crosses, and MA93 emission-line stars are shown as circles with 1″ radius. The edge of the ACIS field is visible in left panel, and images are elongated due to distance from *Chandra*'s aim point.

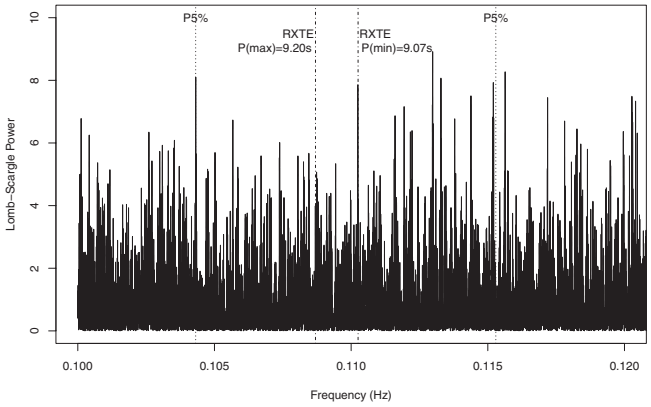

Figure 5. CXOU J004913.5-731138 = SXP9.13. This known HMXB pulsar was detected with >1000 counts, but pulsations were not seen. The power spectrum shows many noise peaks of similar size over the period range $P \pm 5\%$. Further restricting the domain of interest to the period range seen by *RXTE* does not single out any identifiable modulation.

below the detection threshold of *RXTE* nor has it spun down appreciably. The orbital phase (Table 5) for SXP172 on MJD 54061 was 0.32 (L05 ephemeris), placing it reasonably far from peak phase. This pulsar has historically been seen in outburst at times uncorrelated with the X-ray and optical period.

5.8. CXOU J005153.2-723148–SXP8.88

The *Chandra* source has a *ROSAT* counterpart (PSPC No. 265) in Table 7 (RX J0051.8-7231) and is a known Be X-ray pulsar (Corbet et al. 2004). The CXOU coordinates are consistent with the optical counterpart (No. 506 in MA93), which also appears in the MCPS ($V = 14.38$ mag, $B-V = 0.41$ mag). SXP8.88 was detected in our data with 183.8 net ACIS-I counts, exhibiting a hard spectrum and $L_X = (1.46 \pm 0.13) \times 10^{34}$ erg s^{-1}. The median photon energy ($E_{50} = 2.32$ keV) and quantiles ($QDx = -0.45$, $QDy = 1.06$) imply a power-law index $\Gamma \sim 1$. The pulse-period history of SXP8.88 is known to high accuracy from *RXTE* studies (G08). Accordingly, we searched the period range 8.5–9.5 s, finding the highest peak at $P = 8.89909$ s, within the 0.889–0.915 s variation seen by *RXTE*. The periodogram and folded light curve appear in Figure 10. The orbital phase was 0.82 according to the G08 ephemeris (Table 5) placing this detection outside of the normal range of outbursts, which accounts for the faint flux.

5.9. CXOU J005205.6-722604–SXP7.78–SMC X-3

The source was detected in DF1 at coordinates consistent with SMC X-3. With 72 net counts, the point-source detection is highly significant and yields accurate position and quantile information. Neither the LS nor the three alternative periodograms (Z-statistic, epoch-folding, MHP) show any evidence for 7.78 s pulsations. Instead they show a peak at 448 s which however has a significance below 95% based on Monte Carlo simulations or the Press et al. (1992) criteria. Figure 11 shows the periodogram for the expected period range (a 5% range either side of 7.78 s), with the narrow limits of the range seen by G08 with *RXTE* indicated.

The association of SXP7.78 with SMC X-3 was made by Edge et al. (2004) from a Shallow (10 ks) *Chandra* observation of the Bar on 2002 July 20 that detected pulsations with the same period as the *RXTE* pulsar SXP7.78. The more accurate *Chandra* position confirmed the association of this source with the emission-line star MA93 No. 53 (Edge et al. 2004, which lies at the same coordinates as the SMC X-3 optical counterpart proposed by Crampton et al. 1978). Our 2006 detection is consistent with the same counterpart which is also an MCPS star (Table 11).

As shown in Table 6, the *ROSAT* HRI catalog (Sasaki et al. 2000) contains an entry (No. 43) for SMC X-3 that matches a different *Chandra* DFs source (CXOU J005209.2-722553). According to Edge et al. (2004), SMC X-3 lies at R.A. = 00:52:05.7, decl. = −72:26:04 (error radius = 0.″62) and is thus consistent only with CXOU J005205.6-722604 and not CXOU J005209.2-722553. The *ROSAT* HRI source No. 43 was probably SMC X-3 despite the positional offset, owing to its strong variability and the relatively large positional uncertainty (15.″9).

The orbital phase (G08 ephemeris, Table 5) was 0.62 which is within the normal range of outbursts for SXP7.78.

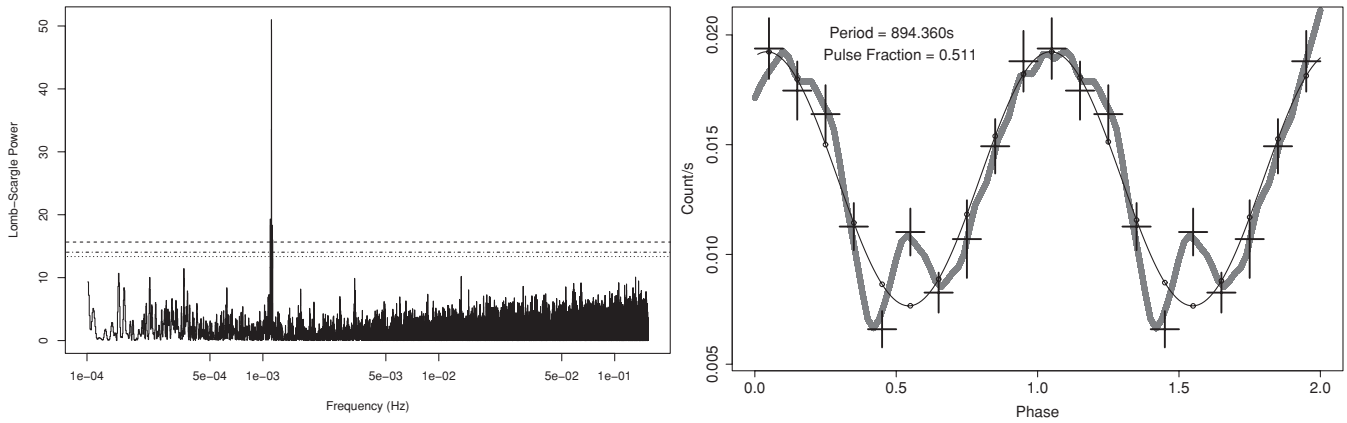

Figure 6. SXP892. New long-period pulsar with $P = 894.36$ s and a sinusoidal profile.

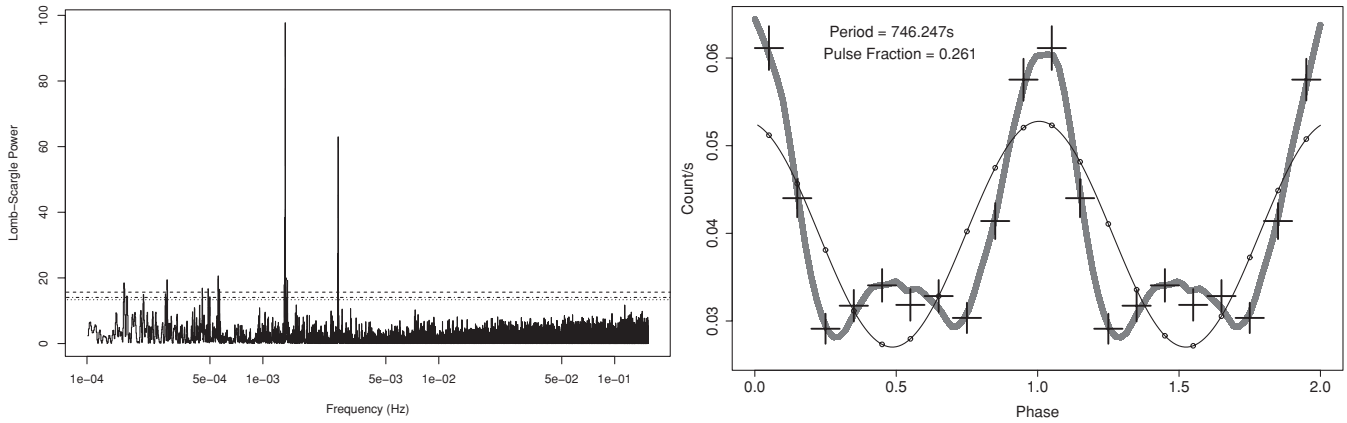

Figure 7. SXP756. Detected with $P = 746.25$ s. The power spectrum shows a strong first harmonic, indicative of a non-sinusoidal modulation. The folded pulse profile exhibits a distinct secondary peak 180° out of phase with the narrow main pulse.

5.10. CXOU J005209.2-722553

This source appears in Table 6 as a spurious positional coincidence to a *ROSAT* HRI detection of SMC X-3. CXOU J005209.2-722553 is an unrelated source lying several arcseconds away from the established position of SMC X-3, based on the identification of its optical counterpart (Edge et al. 2004). CXOU J005209.2-722553 was detected in the DF1 data set with 14.4 ACIS-I net counts, corresponding to a flux $F_{Bc} = (2.4 \pm 0.9) \times 10^{-15}$ erg cm^{-2} s^{-1}. The median photon energy $E50 = 1.56$ keV and quantiles ($QDX = -0.71$, $QDY = 1.1$) suggest a spectrum consistent with power-law photon index $\Gamma = 1.5$–2 keV and moderate absorption $N_{\rm H} \sim 5 \times 10^{21}$ cm^{-2} (Figure 20). There is no optical counterpart in MA93 or MCPS, which together with the X-ray properties suggests a background AGN.

5.11. CXOU J005214.0-731918–SXP15.3

DF2 (Figure 3) registered a clear detection of a point source at the coordinates of the SXP15.3 optical counterpart identified by Edge (2005). We detect 147 net ACIS-I counts, corresponding to a luminosity $L_x = 6.77 \times 10^{33}$ erg s^{-1}. There is no X-ray ephemeris for SXP15.3, but Edge (2005) produced an ephemeris ($P = 75$ days) from optical photometry of the counterpart. Accordingly, the orbital phase was 0.13 on MJD 54061.

CXOU J005214.0-731918 matches the *ROSAT* HRI source No. 44 (Sasaki et al. 2000) and *ASCA* source No. 43 Yokogawa et al. (2003), both of which are identified as the HMXB pulsar RX J0052.1-7319 = SXP15.3. Table 6 shows that this object was also associated with PSPC source No. 453 by Sasaki et al. (2000) based on the overlapping error radii of the two *ROSAT* instruments. The PSPC source does not appear in Table 7 as the *Chandra* coordinates lie beyond the combined PSPC and *Chandra* 95% positional uncertainty.

Having confirmed CXOU J005214.0-731918 as SXP15.3 on positional grounds, we identified weak pulsations at $P = 15.239$ s. The range of periods seen by G08 with *RXTE* is indicated in Figure 12 by two vertical lines. The minimum pulse period recorded by *RXTE* was 15.23 s, on MJD $\sim$ 53950, approximately 110 days before the *Chandra* observation. Prior to this, *RXTE* has shown a steady 3 year long spin-up, with the longest period ($P = 15.27$ s) recorded on MJD $\sim$ 52900. The peak detected in our *Chandra* light curve at $P = 15.239$ s is thus in close agreement with the most contemporaneous *RXTE* detection. Alternatively, the *Chandra* result can be regarded as an upper limit on the pulsed flux.

Another separate source, CXOU J005215.4-731915, was detected just 7.5 arcsec away from SXP15.3, as can be seen in Figure 3. Haberl et al. (2008) have reported an *XMM-Newton* detection of SXP15.3 which actually better matches the nearby source. The situation is clarified by Figure 13.

Our *Chandra* coordinates for this object place it 7.5 arcsec away from an *XMM-Newton* source identified with SXP15.3 by Haberl et al. (2008). However, as shown in Figure 13 the error circle of the *XMM-Newton* source is inconsistent with CXOU J005214.0-731918. This in combination with the fact that the latter shows tentative periodicity at $P \sim 15.24$ s and is associated with both an emission-line counterpart (No. 552 in MA93)

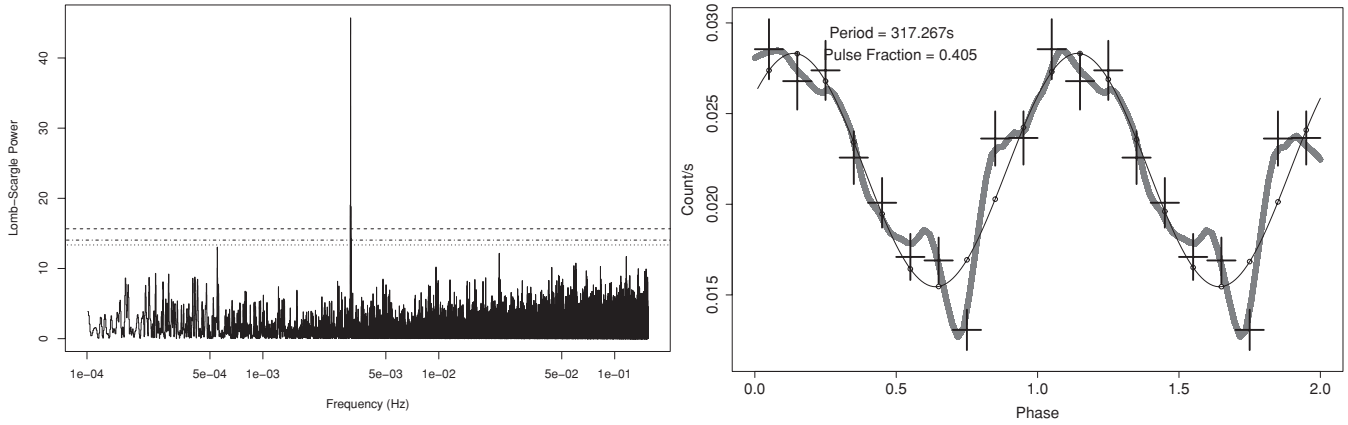

Figure 8. SXP323. Detected with $P = 317.3$ s at the lower boundary of the period range seen by *RXTE*. The pulse profile is remarkably similar to that of SXP326.

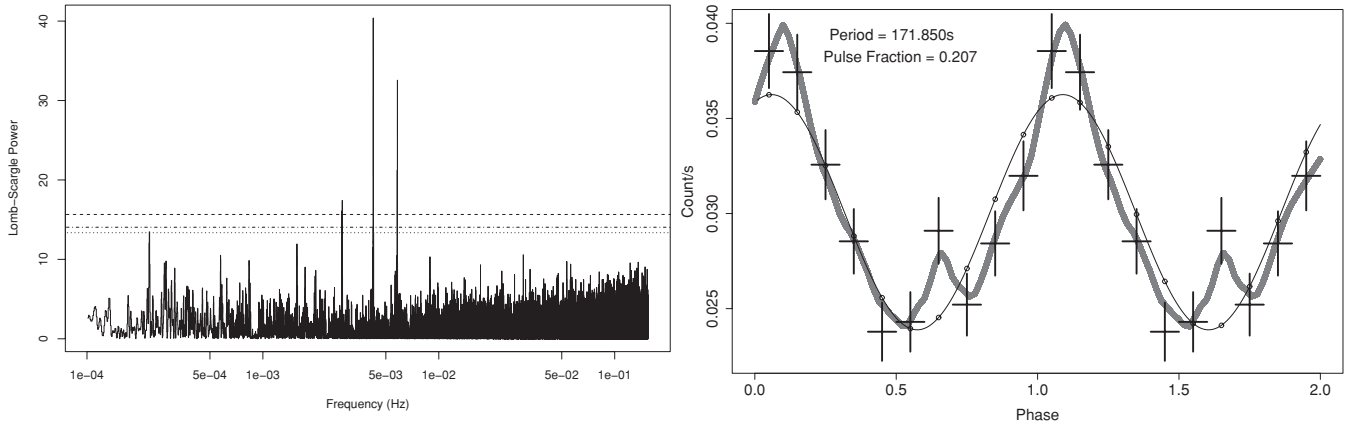

Figure 9. SXP172. Detected with pulse period $P = 171.8$ s. The source lies close to the outer edge of the ACIS CCD, and the additional peak in the PDS at 235.8 s is close to 1/3 the *Chandra* ACIS *Z*-axis dither period of 707 s. It could alternatively be a second pulsar within the *Chandra* PSF.

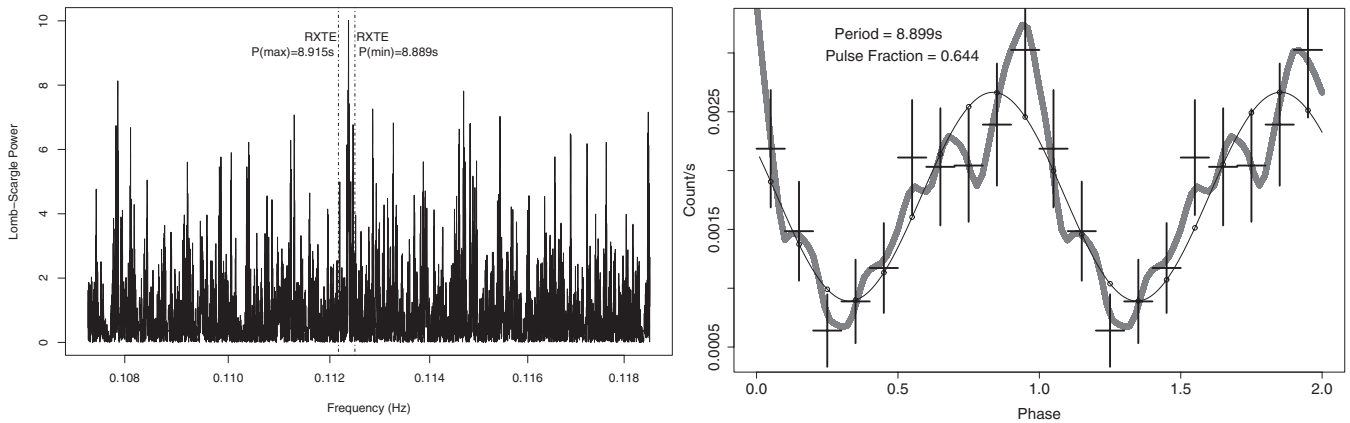

Figure 10. SXP8.88. The pulsar was detected at $P = 8.89909$ s, which is within the narrow range of pulse periods seen by Galache et al. (2008) with *RXTE*, indicated by vertical lines.

and the *ROSAT* HRI source No. 44 strongly suggests that it is SXP15.3. Meanwhile, the nearby source CXOU J005215.4-731915 is positionally coincident with the *XMM-Newton* source, strongly suggesting that these represent an unrelated object.

5.12. CXOU J005215.4-731915

The superb angular resolution and PSF of *Chandra* enabled a clean discovery of this source, which is a very close neighbor of SXP15.3. The two objects are separated by only 7.5 arcsec. At the time of our *Chandra* observation, CXOU J005215.4-731915 was brighter than SXP15.3. This indicates that J005215.4 is strongly variable and that it is active much less frequently than SXP15.3. The *Chandra* coordinates are a positional match to an *XMM-Newton* source (Table 9) that was reported by Haberl et al. (2008) who, in the absence of pulsations, associated it with SXP15.3. As Figure 13 shows, the *XMM-Newton* detection is more consistent with an independent discovery of CXOU J005215.4-731915. There is also a PSPC source (No. 453) that lies almost equidistant from both objects.

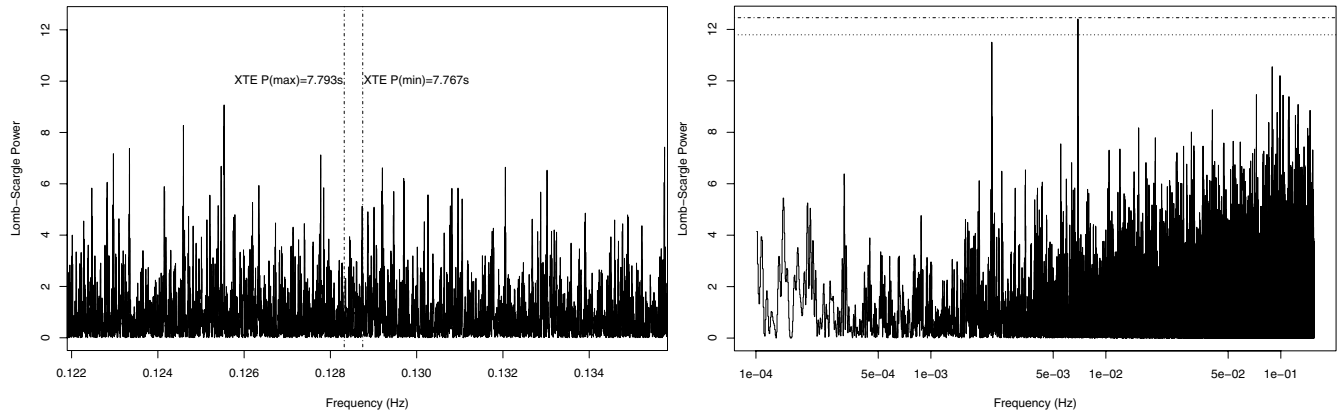

Figure 11. SMC X-3 = CXOU J005205.6-722604 = SXP7.78. Left panel: this source shows no detectable pulsation within the range of the *RXTE* pulse-period history (bounded by vertical lines); the frequency range shown spans 7.78 s ± 5%. Right panel: a blind search of the light curve produced a peak at 448 s which is probably false and does not reach the 95% significance level derived by Monte Carlo.

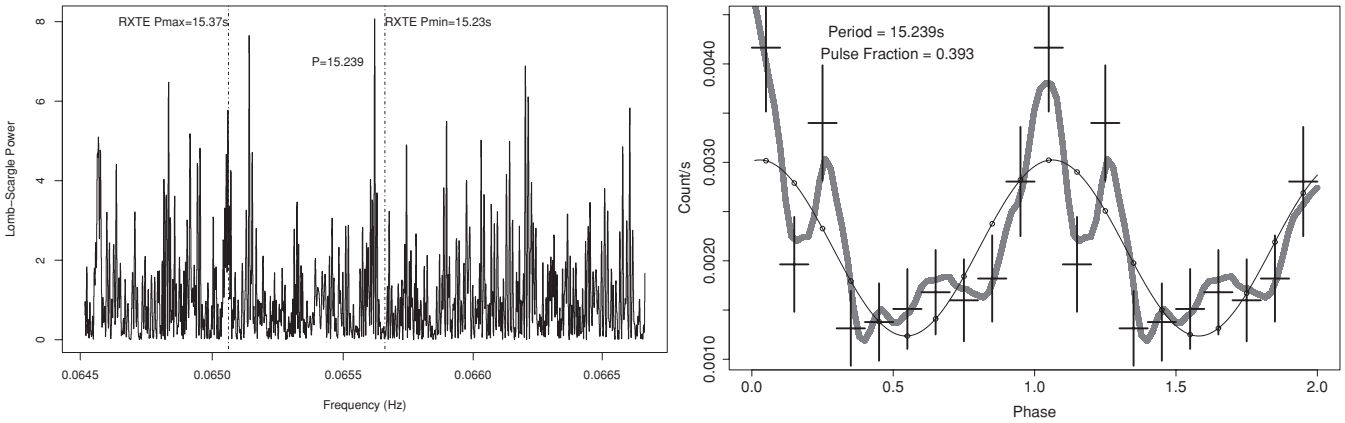

Figure 12. SXP15.3. We are able to identify weak pulsations thanks to accurate *RXTE* measurements of the pulse period. The range of periods seen by Galache et al. (2008) with *RXTE* is indicated by two vertical lines. The *RXTE* P(min) value was recorded ∼110 days before the *Chandra* observation. Prior to this, *RXTE* showed a 3 year long spin-up from P(max). The peak at $P = 15.239$ s is thus consistent with the most contemporaneous *RXTE* detection. More conservatively, the data may be interpreted as an upper limit on the pulsed flux.

The source was detected with 286 net ACIS counts (cf. 147 for SXP15.3) and its spectrum (Table 4) well fits a power law ($\Gamma = 0.93 \pm 0.20$) with absorption column ($n_{\rm H} = 0.65 \pm 1.5$ cm^{-2}) consistent with SMC pulsars. The X-ray flux of 1.13×10^{-13} erg cm^{-2} s^{-1} corresponds to $L_X = 4.86 \times 10^{34}$ erg s^{-1} in the SMC.

There is a bright optical counterpart in the MCPS catalog ($V = 15.90$ mag, $B - V = -0.14$ mag) with magnitude and color consistent with an early-B spectral type. The counterpart, spectrum, and long-term variability all point to an HMXB. Further observations are required to either detect X-ray pulsations or otherwise constrain its nature.

5.13. CXOU J005252.2-721715–SXP326

This is a new pulsar discovered in DF1. The X-ray pulsar was in a bright outburst state with 9292 net ACIS-I counts, and consequently the 326 s pulsation is detected at very high significance as shown in Figure 14. The derived luminosity is $L_x = 5.5 \times 10^{35}$ erg s^{-1}, consistent with a moderate type I (normal) outburst from a Be XRB pulsar. The ACIS spectrum in the 0.3–8 keV band is well fit by a power law with photon index $\Gamma = 1$, with very low extinction (Table 4). DF1 is monitored regularly by *RXTE*, which has never detected SXP326, therefore either the pulsar is rarely in outburst or its normal outbursts are always below the *RXTE* pulsed flux detection limit of $\sim 10^{36}$ erg s^{-1}. The source was also detected by *XMM-Newton* and proposed as a Be-HMXB pulsar with period 325 s by Haberl et al. (2008; XMMU J005252.1-721715). The *XMM-Newton* and *Chandra* coordinates are separated by 0.″66, within an error budget of 1.″93 (quadrature sum of 95% statistical and systematic errors for both telescopes).

SXP326 is associated with an early-type star in the MCPS catalog with photometric parameters consistent with those of Be stars.

5.14. CXOU J005323.8-722715–SXP138

Based on its coordinates and the detection of 138 s pulsations, this source is confirmed as SXP138. In addition to the previously known pulse period of 138 s, we detected a number of other periods (Figure 15). We note that the 138 s period contained the most power as shown in Figure 15. Analysis of the combined light curve of both observations revealed highly significant periods at 500.00, 333.33, 161.29, and 138.88. The exact factors (500, 333.33) of the *Chandra* Y-axis dither period (1000 s) suggest that at least some of these periods are due to the source being moved back and forth across a chip edge or node boundary. Indeed, CXOU J005323.8-722715 lies within 10″ of the CCD's edge. It is not easy to see why the remaining periods (972, 161, and 138) should follow a separate geometric relation, unless one of them is a pulse period and the others are harmonics.

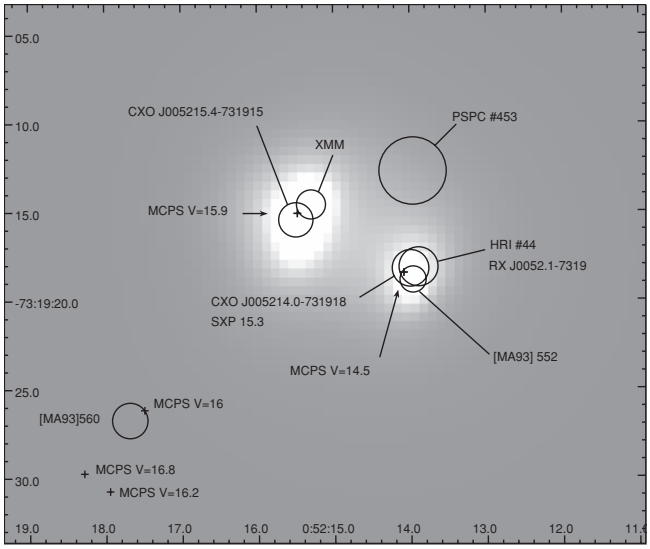

Figure 13. *Chandra* ACIS image of the XRB SXP15.3 (RX J0052.1-7319), and the nearby source (CXOU J005215.4-731915) which is a new HMXB candidate. Labeled circles indicate positional error radii for *Chandra*, *ROSAT*, and *XMM-Newton* detections. The *XMM-Newton* source was reported by Haberl et al. (2008) who associated it with SXP15.3; we find that it is likely an independent discovery of the new HMXB candidate. Bright stars ($V < 17$) in the MCPS catalog are indicated by crosses, and MA93 emission-line stars are shown as circles with 1″ radius. Both SXP15.3 and CXOU J005215.4-731915 have optical counterparts, while only three other bright stars appear in this 0.5 arcmin field, indicating that the chance of random coincidence is small.

Careful analysis of the two individual 50 ks sub-observations and the full light curve shows that although both segments alone show a 138 s period modulated at ∼972 s, the phase of the long periodicity is different in the two obsids and in consequence is totally suppressed in the full light curve. We conclude that the additional periods are an interaction between the pulse period and *Chandra*'s dither. At the time of the DF1 observation (MJD 53851), SXP138 was at orbital phase 0.005 (G08 ephemeris, Table 5), which is the point of minimum flux, and assumed to be far from periastron. The luminosity of the pulsar at this presumable low state is 2.25×10^{35} erg s^{-1} with a PF = 0.46.

5.15. CXOU J005331.7-722240

This source is sufficiently bright (386 net ACIS counts) for spectral fitting and timing analysis. We found a (LS) periodogram peak at $P = 131.11$ s that meets our initial criterion of the 90% significance level from the formula of Press et al. (1992; see Figure 16). More accurate significance levels were then computed via Monte Carlo simulation (as described in Section 3) which accounts for the statistical and sampling properties of the light curve. The simulations yielded a significance of >95% for the 131.1 s period. There are no other periodicities seen in the light curve making it unlikely that aliasing or beating of a slower modulation is responsible for the peak. The 131.11 s period was confirmed by the MHP, although the MHP highest peak was at $P = 262.234$ which is exactly twice the LS period (MHP often finds the sub-harmonics; Schwarzenberg-Czerny 1996).

The X-ray spectrum is well fit by a power law (Table 4), with index $\Gamma = 1.84 \pm 0.22$, absorbed by a column density $N_{\rm H} \sim 2 \times 10^{21}$ cm^{-2}. The X-ray flux (2–10 keV) was $f_x = 6.3 \times 10^{-14}$ erg cm^{-2} s^{-1}, which if located in the SMC corresponds to $L_X \sim 2.7 \times 10^{34}$ erg s^{-1}. There is no prior detection of an X-ray source at these coordinates in the literature, although if active at this level it could have been detected by *XMM-Newton* or *Chandra* (in the Shallow survey), indicating variability.

We do not find any counterparts to this source in the MCPS catalog down to $V < 20$ mag, similarly, we do not find any counterparts in the MA93 catalog, which appears to rule out an HMXB. As the periodicity does not reach 99% significance, it could be a false period, driven by actual but aperiodic variability in the light curve. The power-law index is suggestive of an AGN.

5.16. CXOU J005352.5-722639

This new HMXB candidate appears in Table 7 as one of three positional counterparts for PSPC source No. 242 (RX J0053.9-7227). The separation is 21.″52 with an error budget of 25.″71 (the CXOU positional error is 0.″51 as the source fell close to the *Chandra* aim point). The *ROSAT* source has been identified as the 46.6 s *RXTE* pulsar XTE J0053-724 by CML98, which has since been pinpointed by McGowan et al. (2008) to a location that is consistent with CXOU J005355.3-722645 (see Section 5.18 for SXP46.6). Thus, the association of PSPC No. 242 with CXOU J005352.5-722639 is spurious; however, there is more to the story.

There is a probable optical counterpart to CXOU J005352.5-722639, an emission-line star (No. 717 in MA93) that is consistent with our *Chandra* error circle. The separation between the MA93 and CXOU coordinates is 0.″84, which is less than the quadrature sum of the 95% positional error radius (0.″513) and the *Chandra* aspect uncertainty (a total error budget of 0.″91).

Buckley et al. (2001) reported finding two Be stars in the *ROSAT* PSPC error circle of the source PSPC No. 42 = SXP46.6.

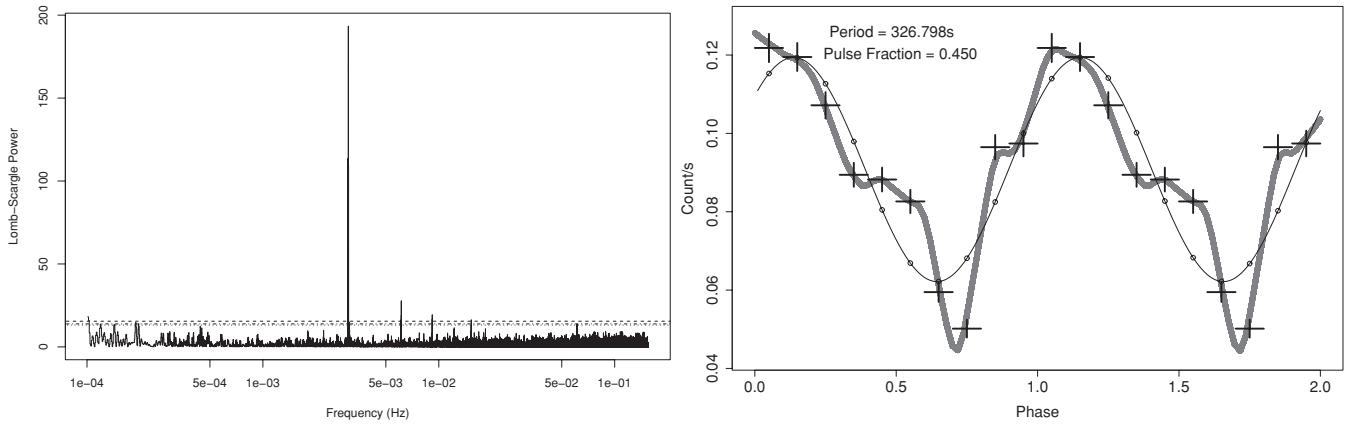

Figure 14. SXP326. New pulsar, $P = 326.8$ s. Several harmonics appear in the power spectrum and the pulse profile shows a high degree of structure.

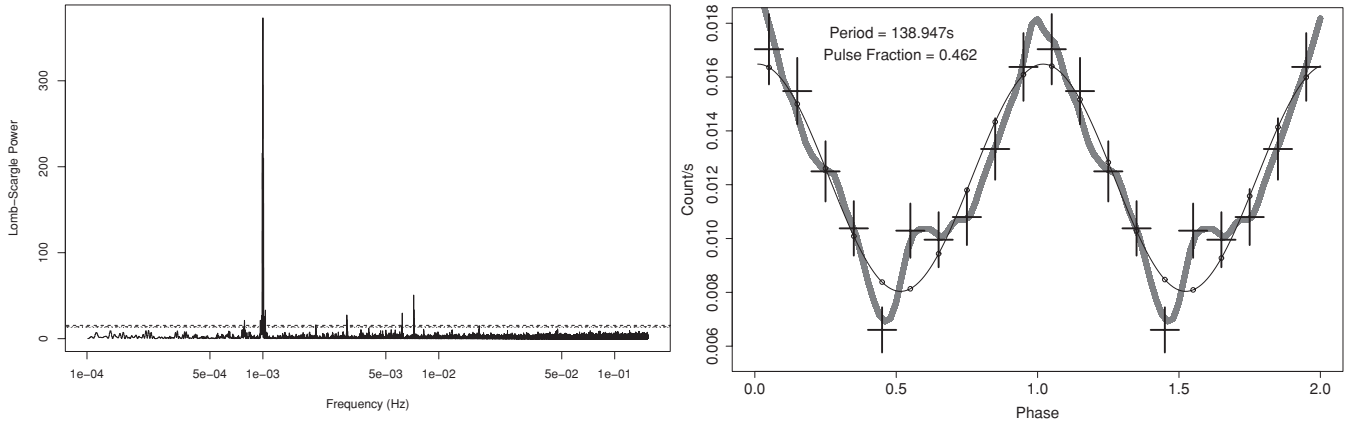

Figure 15. SXP138. Detected with pulse period $P = 138.9$ s. The source was close to a CCD boundary in the ACIS detector, causing the additional peaks in the PDS (e.g., at 1000.0 s) that are artifacts of *Chandra*'s dither pattern.

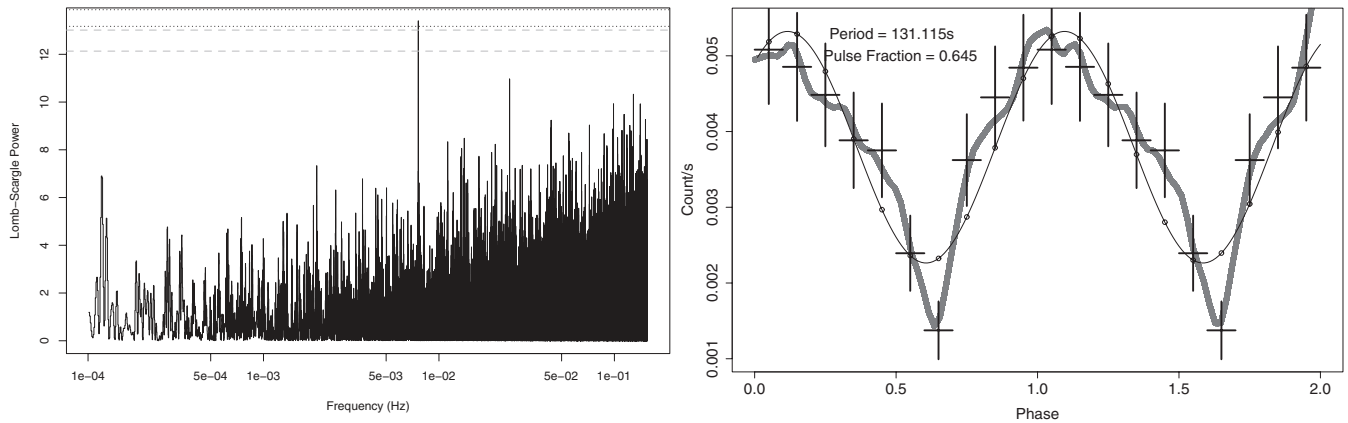

Figure 16. CXOU J005331.7-722240 exhibits a candidate period of $P = 131.11$ s. Detection significance levels 90% and 95% derived by Monte Carlo simulation for a blind search over the period range 6–10,000 s are indicated by dashed lines, while those from the formula of Press et al. (1992) is dotted.

These were referred to as "Eastern Component of Star A and Star B." The correct counterpart to SXP46.6, "Star B" was identified by McGowan et al. (2008), based on its optical variability period matching the *RXTE* ephemeris of the pulsar.

We have discovered that CXOU J005352.5-722639 and [MA93]717 are both coincident with "Eastern Component of Star A," thus the deprecated counterpart turns out to be a separate HMXB candidate in its own right. There is no MCPS match to this object, but Buckley et al. (2001) show it to be a B1e–B2e star with $V = 14.2$ mag and a variable infrared excess.

For this faint *Chandra* source (9.5 ACIS-I net counts), we measured an X-ray flux $F_{Bc} = (1.2 \pm 0.6) \times 10^{-15}$ erg cm^{-2} s^{-1}, corresponding to $L_X = 5.2 \times 10^{32}$ erg s^{-1}. The quantile values ($QDx = -0.2$, $QDy = 0.9$, see Figure 20 for model grid) and median photon energy ($E50 = 3.2$ keV) suggest a hard source, with little ($<10^{21}$ but poorly constrained) absorption.

In summary, CXOU J005352.5-722639 is a new HMXB candidate based on its hard X-ray spectrum and Be-star counterpart. It has not been detected in outburst and no pulsations have been seen.

5.17. CXOU J005354.8-722722

This source (with 17 ACIS net counts) appears in Table 7 as one of three positional counterparts for PSPC source No. 242 (RX J0053.9-7227). The separation is 22.″78 with an error budget of 25.″70. We measured an X-ray flux $F_{Bc} = (2.3 \pm 0.7) \times 10^{-15}$ erg cm^{-2} s^{-1}, corresponding to $L_X = 1.0 \times 10^{33}$ erg s^{-1}. The quantile values ($QDx = -0.34$, $QDy = 1.58$, see Figure 20 for model grid) and median photon energy ($E50 = 2.70$ keV) suggest a hard source with high absorption column density ($N_{\rm H} > 10^{22}$ cm^{-2}). A likely interpretation is a background AGN.

5.18. CXOU J005355.3-722645–SXP46.6

McGowan et al. (2008) have identified the frequently active 46.6 s pulsar XTE J0053-724 (Marshall et al. 1997) with one of two optical counterparts ("Star B") proposed by Buckley et al. (2001), using archival *Chandra* data (including the DF1 data set). McGowan et al. (2008) discovered that the optical counterpart of the *Chandra* source exhibits a photometric period of $P = 136$ days which matches the X-ray outburst based ephemeris derived by the *RXTE* monitoring project for SXP46.6 (L05, G08), although *Chandra* has not seen the 46.6 s pulsations.

We detect this source with 63 net ACIS-I counts and $F_{Bc} = (5.4 \pm 0.8) \times 10^{-15}$ erg cm^{-2} s^{-1} corresponding to $L_X = 2.3 \times 10^{33}$ erg s^{-1}. The median photon energy ($E50 = 1.61$ keV) and quantiles ($QDx = -0.69$, $QDy = 1.30$) imply a medium-hard spectrum, consistent with power-law index $\Gamma = 2$–2.5 and absorption column $n_{\rm H} \sim 5 \times 10^{21}$ cm^{-2}. The power-law index is rather soft for an HMXB pulsar, however, the identification is secure owing to the detection of a 136 day orbital modulation in the pulsar and the optical counterpart. According to the well-defined *RXTE* ephemeris of G08, the orbital phase of SXP46.6 was 0.336 at the time of the DF1 exposure. As has been noted

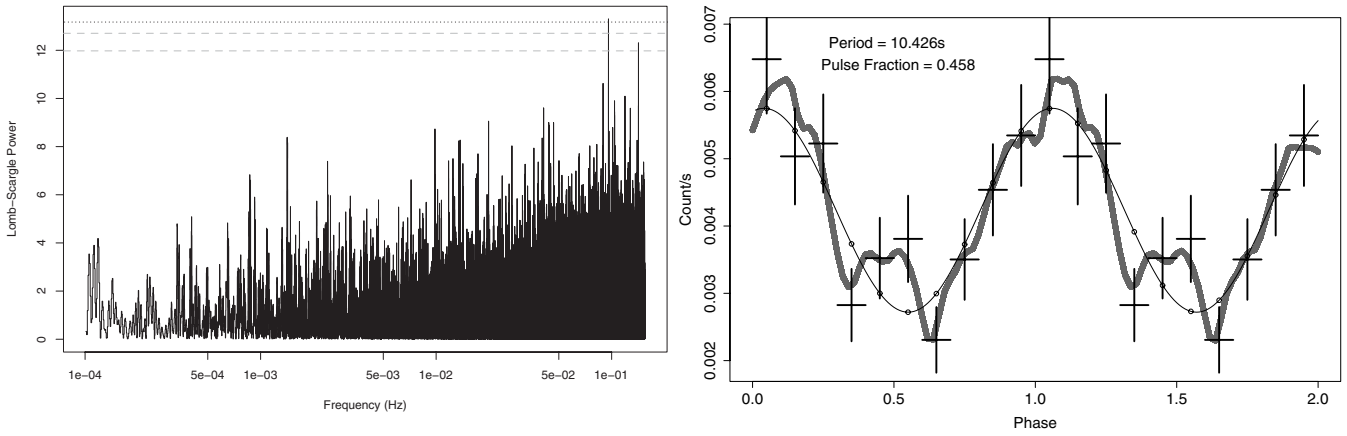

Figure 17. CXOU J005437.1-722637 exhibits a candidate period of $P = 10.426$ s. Detection significance levels 90% and 95% derived by Monte Carlo simulation for a blind search over the period range 6–10,000 s are indicated by dashed lines, while the 90% level from the formula of Press et al. (1992) is dotted.

by McGowan et al. (2008), this would be consistent with low luminosity as the pulsar was far from periastron.

Table 7 shows that the *ROSAT* catalog entry for SXP46.6 (PSPC No. 242, RX J0053.9-7227; Haberl et al. 2000) has a large positional uncertainty and consequently is also coincident with two other DF1 sources (CXOU J005354.8-722722 and CXOU J005352.5-722639), which are discussed separately.

5.19. J005403.9-722633–XMMU J005403.8-722632–SXP342

This source is coincident with a 342 s Be-HMXB pulsar recently proposed by Haberl et al. (2008; XMMU J005403.8-722632). The separation between the CXOU and *XMM-Newton* coordinates is just 0.″27, within a combined error budget of 1.″93 (the quadrature sum of the 95% statistical and systematic errors for both telescopes). We detected SXP342 with only 36 net ACIS-I counts, which is insufficient for timing analysis. The 0.3–8 keV flux $F_{Bc} = 8.8 \times 10^{-15}$ erg cm^{-2} s^{-1} corresponds to a luminosity of $L_X = 3.8 \times 10^{33}$ erg s^{-1}. The median photon energy ($E50 = 3.4$ keV) and quantiles ($QDx = -0.17$, $QDy = 0.89$) imply a very hard spectrum, consistent with power-law index $\Gamma < 0.5$ and low absorption column $N_{\rm H} \leqslant 10^{21}$ cm^{-2}. Similarly, Haberl et al. (2008) reported that the *XMM-Newton* spectrum during outburst was the hardest of any Be-XRB in the SMC. They also note that SXP342 cannot be unambiguously identified with the pulsar SXP348 tracked by the *RXTE* monitoring project (G08), which may be an amalgam of SXP342 and SAX J0103.2-7209 ($P = 345$ s), as both lie within the same *RXTE* field of view.

5.20. CXOU J005428.8-722810, CXOU J005433.0-722806, and CXOU J005436.5-722816–RX J0054.5-7228

Three DF1 sources (Table 7) fall in the positional error circle of *ROSAT* PSPC source No. 248 (RX J0054.5-7228). Haberl & Sasaki (2000) point out that six emission-line objects from the catalog of MA93 lie in the error circle. We found that none of the three *Chandra* sources have an MA93 counterpart, using a search radius equal to the *Chandra* 95% error circle in quadrature with 0.″75 aspect uncertainty and 5″ tolerance on the MA93 coordinates. Thus, no positive identification can be made with RX J0054.5-7228.

5.21. CXOU J005437.1-722637

This source was sufficiently bright (433 net ACIS counts) for spectral fitting and timing analysis. We found an LS periodogram peak at $P = 10.426$ s that meets our initial criterion of >90% significance (see Figure 17). More accurate significance levels were then computed via a Monte Carlo simulation (as described above) which accounts for the statistical and sampling properties of the light curve. The simulations yielded a significance >95% for the 10.426 s period, which is not an integer multiple of the ACIS readout (3.2 s). There are no other periodicities seen in the light curve making it unlikely that aliasing or beating of a slower modulation is responsible for the peak. Alternative methods including the MHP (Schwarzenberg-Czerny 1996), epoch folding, and *Z*-statistic did not find this peak, making the detection questionable.

The X-ray spectrum is well fit by a moderate power law, with index $\Gamma = 1.81 \pm 0.21$, absorbed by a column density $N_{\rm H} \sim 10^{21}$ cm^{-2}. The X-ray flux (0.3–8 keV) was $F_{Bc} = (4.6 \pm 0.2) \times 10^{-14}$ erg cm^{-2} s^{-1}, which if located in the SMC corresponds to $L_X \sim 2 \times 10^{34}$ erg s^{-1}. There is no prior detection of an X-ray source at these coordinates in the literature, although if active at this level it could have been detected by *ROSAT*, *XMM-Newton*, or *Chandra*, from which we infer it is variable.

We do not find any stars in MCPS down to $V \sim 20$ mag, or emission-line objects in the MA93 catalog, within the *Chandra* error circle. This in combination with the marginal period detection and relatively soft X-ray spectrum (for an X-ray pulsar) suggests that the source is not an HMXB and is likely an AGN.

5.22. CXOU J005446.3-722523–Candidate HMXB P = 4693 s

This source lies in DF1 (Figure 2) and was detected with 140 net counts. The median energy ($E50 = 2.24$ keV) indicates that the source is hard, and X-ray quantiles ($QDx = -0.47$, $QDy = 1.13$) show the spectrum to be consistent with an absorbed power law (photon index $\Gamma \sim 2$, $N_{\rm H} \sim 10^{22}$ cm^{-2}). The flux $F_{Bc} = (2.1 \pm 0.2) \times 10^{-14}$ erg cm^{-2} s^{-1} results in $L_X = 9 \times 10^{32}$ erg cm^{-2} s^{-1} if located in the SMC.

Timing analysis (Figure 18) revealed a very long periodic modulation at $P = 4693$ s, which exceeded the 99% significance level derived by Monte Carlo and the formula of Press et al. (1992) for the LS periodogram. Alternative methods (the *Z*-statistic, epoch folding, and MHP) confirmed the 4693 s period. The periodogram and folded light curve are shown in Figure 18.

The source has a bright MCPS optical counterpart as shown in Table 11 which lies well within the *Chandra* 95% error radius

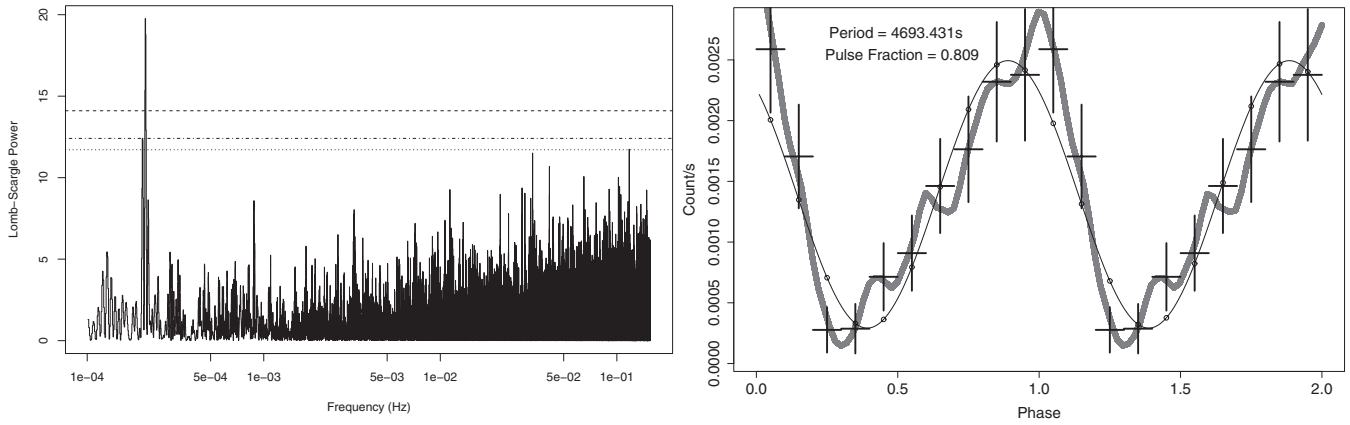

Figure 18. CXOU J005446.3-722523. The period detected at $P = 4693$ s exceeds the 99% significance level derived by Monte Carlo and is confirmed by other algorithms. The source has a $V = 15.36$ optical counterpart making it a likely HMXB. If confirmed this would be the longest period pulsar known.

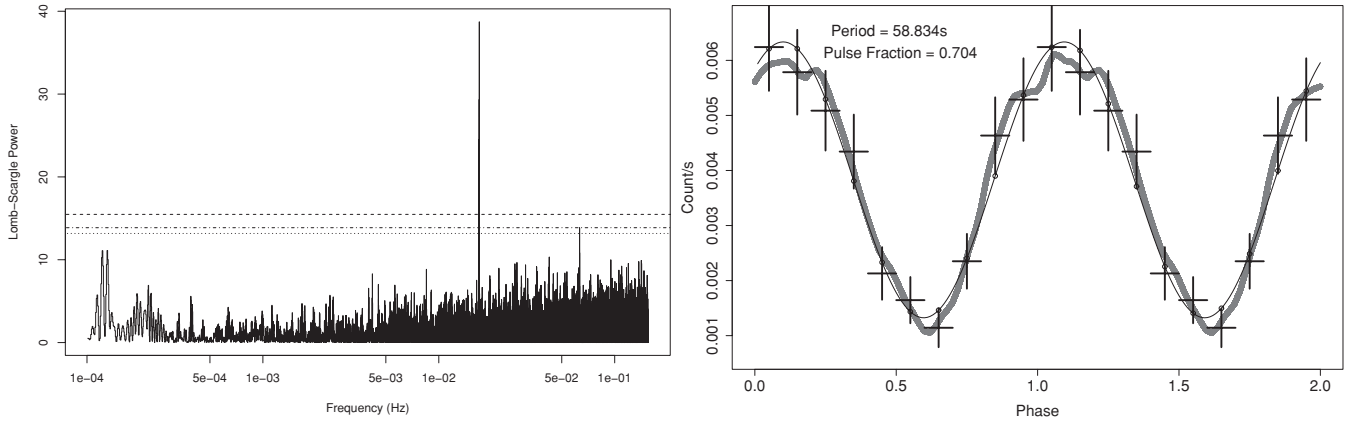

Figure 19. SXP59. Pulse period was $P = 58.8$ s. The profile is very close to perfectly sinusoidal although a harmonic is detected.

(0.″94, the quadrature sum of 0.″56, and the aspect uncertainty 0.″75), at a separation of 0.″55. The counterpart has a magnitude $V = 15.36$ mag and color indices $B - V = 0.14$ mag, $U - B = -1.11$ mag, and $V - I = 0.109$ mag. At the distance of the SMC (60 kpc), the absolute magnitude is $M_V = -3.53$, which together with the $U - B$ color implies a spectral type of B0V–B1V. The emission-line star [MA93]798 (Table 10) is also associated with the source. With this counterpart, the object is a likely Be-HMXB, which would make it the longest-period HMXB pulsar to be discovered. The implications of such a long-period pulsar are discussed in Section 7.2.

5.23. CXOU J005456.1-722648–SXP59

The source was detected in the *Chandra* observation of DF1 (Figure 2) at a luminosity of 1.83×10^{34} erg s^{-1} with pulse period 58.8 s (Figure 19). According to the G08 ephemeris, SXP59 was at orbital phase 0.65 during the DF1 observation on MJD 53851, which is within the range for normal outbursts seen in SXP59. We measured a pulse period of 58.85815 s which is longer than the last reported measurement by G08 on MJD 54000, but in line with the long-term average value. SXP59 tends to spin up when in outburst and spin down in quiescence.

6. DEEP FIELDS X-RAY SOURCES WITH BRIGHT STELLAR COUNTERPARTS

We searched for optical counterparts consistent with HMXBs using the emission-line star catalog of MA93 and the MCPS. The MA93 objective-prism survey catalog contains the counterparts to almost all known Be-HMXBs in the SMC. The MCPS is complete for $V < 20$, corresponding to $M_V = 1$ at $D_{\rm SMC} = 60$ kpc, which encompasses the full brightness range of HMXBs. According to McBride et al. (2008), all HMXB counterparts in the SMC have spectral type earlier than B3, thus we restricted our MCPS catalog search to $V < 17$, corresponding to $M_V < -2$. The MCPS counterpart search used the CXOU 95% statistical error circle in quadrature with the aspect uncertainty (0.″75 for 95%). The MA93 counterpart search used the CXOU 95% statistical error circle in quadrature with the aspect uncertainty (0.″75 for 95%) and a 2.″5 tolerance on the MA93 coordinates. The MA93 tolerance was adopted by doubling the largest offset required for an HMXB with an established counterpart (∼1.″2 for SXP59). The fact that emission-line stars are rare and the MA93 plate material dates from the 1970s justifies the larger search region.

There are 18 *Chandra* sources with MA93 counterparts listed in Table 10, of which 9 are confirmed HMXB pulsars, another 2 are *ROSAT* sources. A further seven objects are new discoveries and are denoted by "Be?" in Table 10 as their X-ray emission and emission lines indicate that they are probable Be stars.

There are 40 *Chandra* DF sources with MCPS counterparts brighter than $V < 17$, all unique, listed in Table 11. The MCPS coordinate accuracy is quoted as rms $\sim$ 0.″3, and we found that adding up to 1″ tolerance did not increase the number of matches beyond those contained in the CXOU 95% error circles. Twenty-one of our MCPS counterparts are either confirmed HMXBs and/or are associated with an MA93 star. The confirmed HMXBs and MA93 stars are all blue, having

$B - V < 0.2$ (excepting SXP8.88 which has $B - V = 0.4$). There are a further 12 *Chandra*+MCPS counterparts ("C" in Table 11) that lie in the same range of $B - V < 0.2$, for which the reddest has $B - V = 0.12$. The remaining seven objects are significantly redder, having $B - V = 0.57$–1.89, and are labeled "R" in Table 11.

This bi-modality of the optical color distribution strongly suggests that 33 objects are HMXBs, and the 7 "red outliers" are likely foreground stars and/or random matches. Caution should be exercised in interpretation of the new *Chandra* counterpart identifications as there are other (albeit far rarer) species known to be present in the SMC that could also meet the matching criteria used. In particular, Wolf-Rayet stars, colliding-wind binaries, and supergiant HMXBs all manifest as luminous, blue hard X-ray emitters. Accordingly, a full analysis of the optical counterparts is presented in a companion paper (VA10).

7. DISCUSSION

7.1. Pulsars in the Deep Fields: Number, Orbital Phase, and Pulsed Flux

There were 12 X-ray pulsars known in the survey region prior to these observations, 7 in DF1 and 5 in DF2. The new pulsars SXP326, SXP892, and SXP342 (a faint point source in our data, identified as a pulsar by Haberl et al. 2008) have increased the sample of confirmed pulsars in the region to a total of 15. Most interesting is the fact that we were able to detect all the known pulsars in DF2 and most (5/7) in DF1.

Our observed pulse profiles show a range of forms. The typical profile exhibits significant flux above the un-pulsed component for most of the pulsation cycle. A qualitative distinction exists between profiles that are broad and asymmetric (e.g., SXP326, Figure 14), and those that are strongly peaked which tend to be narrower and more symmetric (e.g., SXP172, Figure 9). These differences are likely due to differences in geometry of the emitting regions (polar caps) of the NS. The literature documents several efforts to model X-ray pulse profiles in terms of combinations of fan and pencil beams (see, e.g., Parmar et al. 1989). Broad and cuspy profiles are attributed to fan beam geometry, where the X-ray beam has the form of a (somewhat irregular) hollow cone, due to obscuration of the central part of the polar cap by the incoming accretion stream, or reflection/re-processing effects. Narrow pulses more closely resemble radio pulsars and are accordingly interpreted in the "light-house" model, as collimated beams (pencil beams) emanating directly from the polar caps. The radiative column, and hence the pulse profile, varies with accretion rate (Karino et al. 2007).

One of the primary objectives of this project was to find out if HMXB pulsars could be detected between outbursts and to determine their quiescent luminosity. Using the latest X-ray ephemerides produced by the *RXTE* monitoring program (G08), we calculated the (presumed orbital) phase of each pulsar at the time of the *Chandra* DF observations (Table 5). The ephemerides were constructed from pulsed flux light curves spanning about 10 years of weekly *RXTE* observations. As such, they predict the most likely time of X-ray outburst, which is presumed to reflect orbital modulation of the mass-transfer rate from the mass-donor star to the NS (the actual orbital ephemeris is not known for any SMC pulsars except SMC X-1). Of the 10 pulsars in our fields with X-ray ephemerides from *RXTE*, 6 were detected far from their normal range of outburst phase and with luminosity well below outburst levels. Two pulsars (SXP59 and SXP7.78) were detected during their normal orbital phase range for X-ray outbursts.

Table 12
Pulsed Fluxes and PFs

Name	P (s)	$\bar{f}$ (count ks^{-1})	f_p (count ks^{-1})	PF $f_p/\bar{f}$
J005437.1	10.4258	4.26	1.95 ± 0.819	0.458
J005331.7	131.115	3.87	2.50 ± 0.732	0.645
SXP138	138.947	12.3	5.67 ± 1.39	0.462
SXP326	326.798	91.2	41.1 ± 3.85	0.450
SXP59	58.8336	3.86	2.72 ± 0.714	0.704
J005446.3	4693.43	1.44	1.16 ± 0.427	0.809
SXP8.88	8.89909	1.80	1.16 ± 0.549	0.644
SXP172	171.85	30.0	6.20 ± 2.32	0.207
SXP323	317.267	22.0	8.90 ± 1.82	0.405
SXP756	746.247	39.4	10.3 ± 2.63	0.261
SXP892	894.36	13.5	6.89 ± 1.49	0.511
SXP15.3	15.2393	2.16	0.849 ± 0.610	0.393

We found no correlation between orbital phase (Table 5) and the pulsed flux or PF as reported in Table 12. There are five pulsars (SXP8.88, SXP59, SXP138, SXP323, and SXP756) for which both pieces of information are available, their orbital periods range from 28.47 days (SXP8.88) to 389 days (SXP756). It is not surprising that such a small sample cannot reveal a link, as we expect the PF to be a strong function of orbital phase only over intervals when the accretion rate is changing rapidly. These measurements are however valuable for establishing the baseline pulsed flux for the individual pulsars at known positions along their respective orbits.

The X-ray luminosity upper limit for the two known pulsars that were not detected is 1.1×10^{33} erg s^{-1} for SXP4.78 and 1.3×10^{33} erg s^{-1} for SXP82 (10 counts at the aim point, divided by the normalized exposure map at the target location). One of these undetected pulsars (SXP82.4) has an X-ray ephemeris (G08) according to which its phase $\phi = 0.863$ (Table 5) indicates that it was far from the usual time of outburst. None of the known pulsars that were detected as point sources without identifiable modulation at the expected pulse periods lay within ±0.2 of ephemeris phase $\phi = 0.5$ which is defined as the outburst peak by G08. This supports the accepted picture of outbursts occurring close to periastron in the bright, recurrent Be-HMXBs, it also demonstrates that appreciable "quiescent" emission can be detected throughout the orbit.

7.2. Pulsars with Very Long Periods

Several long-period pulsars were detected in our 100 ks *Chandra* observations, including two new examples, SXP892 and CXOU J005446.3-722523. SXP892 is a confirmed X-ray pulsar with typical HMXB optical counterpart; while in Section 5.22, we reported a 4693 s modulation in J005446.3-722523 which also has a bright, early-type optical companion. As the period is far longer than any known SMC pulsars, we discuss the implications for the HMXB population and for accretion physics, of the existence of such a pulsar, and the growing number with $P > 500$ s.

The longest confirmed pulse period in the SMC is $P = 1323$ s for the Be-HMXB pulsar RX J0103.6-7201 (Haberl & Pietsch 2005). A total of nine SMC pulsars have been found with periods in excess of 500 s: 1323 s, 967 s (Haberl et al. 2008), SXP892, RX J0049.7-7323: 756 s, RX J0105.9-7203: 726 s (Eger & Haberl 2008), XMMU J005517.9-723853: 701 s (Haberl et al. 2004), XMMU J005535.2-722906: 645 s, CXOU J005736.2-

721934: 565 s, and CXOU J005455.6-724510: 504 s (Edge et al. 2004). In the Milky Way, two very long period X-ray pulsars with periods >1000 s are known, both of them Be-HMXBs: SAX J2239.3+6116 at $P = 1247$ s (in't Zand et al. 2001), SAX J0146.9+6121 at $P = 1412$ s (Hellier 1994). The longest X-ray period of all belongs to 2S0114+650 at $P = 10{,}008$ s which has a B1 supergiant optical counterpart, although it is uncertain whether its X-ray period is the NS spin period or a periodic variation in the accretion rate, driven by tidal modulation of the stellar wind (Koenigsberger et al. 2006).

X-ray pulsars are the product of close-binary systems containing a pair of massive stars. In the widely accepted model (e.g., Bhattacharya & van den Heuvel 1991), following the supernova, the newly formed NS evolves through three distinct epochs (ejector, propellor, and accretor) characterized by changes to its spin rate, through interaction with the wind of the companion. Initially, the NS spin period ($\ll 1$ s) lengthens rapidly with energy losses dominated by magnetic dipole (and higher order) radiation (ejector phase). In the presence of a mass-losing companion, the spin period lengthens far beyond the (< 8.5 s) regime (Young et al. 1999) occupied by radio pulsars, as the NS enters the propellor phase. Matter intercepting the NS with insufficient angular momentum to be accreted is flung away as it enters the magnetosphere resulting in a braking torque on the NS. Once the NS has spun-down to a critical value, accretion begins and the NS emerges as an X-ray pulsar. Corbet (1984) showed that most X-ray pulsars occupy a spin-orbit equilibrium, which is different for wind-fed and disk-fed systems. Monitoring studies (e.g., Bildsten et al. 1997) reveal that HMXB pulsars alternate between spin-up and spin-down states around their long-term equilibrium value.

The maximum spin period depends on the NS magnetic field, mass-transfer rate, and duration of the propellor phase, and thus involves stellar evolution calculations. Urpin et al. (1998) find that for any realistic HMXB model, there exists a maximum NS spin period of $P_{\rm max} = 500$ s that can be reached in the main-sequence lifetime of the mass donor. The existence of long-period X-ray pulsars challenges accretion theory to explain periods that greatly exceed this limit.

A theoretical investigation into long-period X-ray pulsars by Ikhsanov (2006) postulated a modification to NS spin evolution that divides the propellor phase into supersonic and subsonic propellor phases. They report that this refinement removes the ~500 s barrier in specific circumstances and reconciles the standard theory of close-binary evolution with the undoubted existence of long-period HMXB pulsars. Ikhsanov (2006) also gives two scenarios that lead to X-ray pulsars with periods >1000 s. First, if the NS accretes spherically the spin-orbit equilibrium period is an order of magnitude longer than for disk-fed accretion. Second, if the mass-donor star has recently increased its mass-loss rate, a slow-rotating NS companion (that had spun-down to equilibrium spin in a more tenuous wind) will be re-activated as a long-period X-ray pulsar.

Pulsars with periods longer than 1000 s are difficult to identify for two main reasons: they are likely to be faint due to low accretion rates, and their wide orbits mean that outbursts will be infrequent. In addition, long ($\gg$1000 s) observations are needed to unambiguously discern such long periods even in bright sources. Although *RXTE* has found that SXP756 has regular outbursts presumably linked to its orbital period (L05), we do not yet know if the much fainter long-period pulsars found by *XMM-Newton* and *Chandra* are periodically active. The pulsars SXP892 (Figure 6), SXP756 (Figure 7), and the putative $P = 4693$ source (Figure 18) exhibit pulse profiles consistent with pencil-beam dominated emission geometry (e.g., Stella et al. 1986) expected at low accretion rates. SXP756 does show some fine sub-structure in the form of an interpulse ~1/10th the strength of the main peak. In contrast, several of the 100–300 s pulsars have wide peaks with complex structures that can exceed the un-pulsed flux level for most of the pulse cycle.

Whether CXOU J005446.3-722523 can be confirmed as a ~4000 s pulsar or not, it is clear that sensitive observations with *Chandra* and *XMM-Newton* are providing a new window onto the long-period tail of the spin distribution. Continued monitoring and optical counterpart studies will be important to reveal whether the spin-orbit equilibrium for trans-$P_{\rm max}$ pulsars differs from pulsars in the < 500 s range, testing the suggestion of Ikhsanov (2006) that different physics comes into play. A large number of hard point sources in the SMC are still unidentified and could plausibly be X-ray pulsars. The difficulty in detecting long-period systems is sufficient to suspect that the period distribution of undiscovered pulsars could depart significantly from the known examples.

7.3. Population Overview from X-ray Quantiles

According to our quantile diagrams (Figure 20), the majority of the confirmed pulsars (with and without detected pulsation in the *Chandra* data) cluster around power law $\Gamma = 1$, and neutral hydrogen column density $N_{\rm H} \leqslant 10^{21}$ cm^{-2}. Several unidentified sources also lie in this region and are therefore consistent with being additional XRB pulsars. In particular, there are two objects with S/N > 10 (one in Field-1 and one in Field-2) whose quantiles are indistinguishable from specific confirmed pulsars within the errors, CXOU J005057.1-731008 (RX J0050.9-7310) and CXOU J005215.4-731915. The nature of these sources in the context of their multi-wavelength counterparts and spectral properties is discussed in VA10. The two stark exceptions to this rule are SXP46.6 ($\Gamma = 2$–2.5) and SXP342 ($\Gamma < 0.5$), the latter is also unusual in being a bright gamma-ray source detected by *Integral* (McBride et al. 2007).

The upper left region of the quantile diagram contains a group of soft sources that extend outside the power-law grid and are consistent with thermal models appropriate for stellar coronae. In the figures, we show a model grid for TB, and the sources occupy a region approximately bounded by plasma temperatures in the range $kT = 0.4$–2 keV and $N_{\rm H} < 10^{21}$ cm^{-2}. We note that grids can be constructed for more sophisticated stellar coronal models such as Raymond–Smith or MEKAL, but the additional parameters become degenerate in the quantile space, and for low count sources they provide no additional information.

A group of sources with very large extinction occupy the upper right corner of the power-law grid. These are likely obscured AGNs with significant internal extinction. The quantile parameters for these AGN candidates are consistent with $\Gamma \sim 1.7$ power-law spectra, typical of the class.

After accounting for stars, obscured AGNs, and confirmed pulsars, we are still left with the majority of our sources. The unknown sources are not randomly distributed in the quantile plane but lie predominantly in the region bounded by $N_{\rm H} \geqslant 10^{21}$ cm^{-2} and $\Gamma \simeq 1$–2 suggesting that they are colliding-wind binaries, shocked-wind early-type stars, and accretion-powered sources in the SMC (XRBs, CVs) and beyond (AGNs). XRB pulsars can exhibit relatively soft quantiles with $\Gamma \sim 2$—see, for example, Figure 3 in McGowan et al. (2007)—so it is plausible for some of these objects to be pulsars

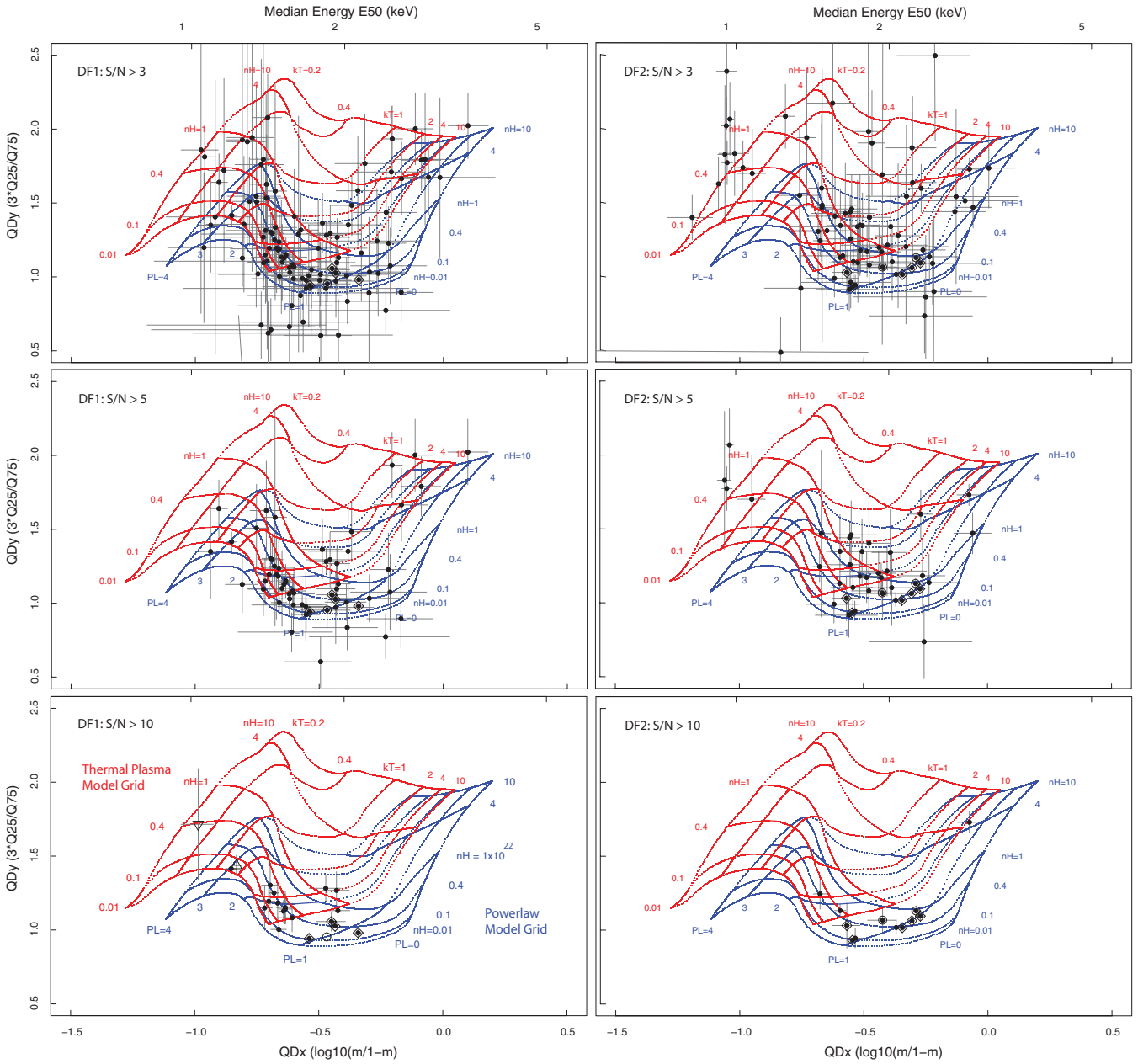

Figure 20. Quantile diagrams for sources in DF1 (left column) and DF2 (right column) with S/N selections of >3, >5, >10 (from top to bottom). Pulsars with detected pulsations in the data are marked by diamonds and those detected without pulsations are marked by circles.

observed in a soft state. CVs and LMXBs are also expected to appear in this region of the quantile diagram. Additionally, CVs and LMXBs are likely to be faint with 0.5–10 keV luminosities in the range 10^{31}–10^{35}, which is consistent with many of these sources. However, the greater proportion of the objects in this group is likely to be background AGNs, which are typically characterized by power-law spectra with $\Gamma \sim 1.7$ and low intrinsic absorption. The expected absorption distribution for background AGNs follows the line-of-sight column through the SMC, which is $N_{\rm H} = (1\text{–}5) \times 10^{21}$ cm^{-2}.

In order to provide a preliminary overview of the content of our *Chandra* SMC DF source catalog (Table 2), we computed an estimate of the proportions and absolute numbers of objects occupying the above-discussed regions of the quantile diagram (Figure 20). The principle is to count the number of high signal-to-noise ratio (S/N > 5) sources populating regions defined for (1) thermal sources with $kT < 1$ KeV, (2) hard-power-law-sources ($\Gamma < 1.2$), and (3) soft-power-law-sources ($\Gamma > 1.5$). In this way, we obtain the fraction of high S/N sources consistent with spectral models that roughly correspond to stars, HMXBs (and colliding-wind stars), and AGNs. Absolute numbers for the fields are then computed by multiplying this fraction by the total size of the catalog down to the completeness limit of our data set. Uncertainties are computed by taking $\sqrt{N}$ of the number of 5σ sources and propagating them to the full sample. We defined a flux limit corresponding 10 count sources at the *Chandra*/ACIS-I aim point in our 100 ks stacked data set, to approximate the completeness limit of our sample. We do this calculation using a flux limited sample because our flux calculations include correction for *Chandra*'s changes in sensitivity and spectral response with distance from the aim point. If a count limit were used instead, it would not be uniform across the field. Each

source has a 0.5–8 keV flux computed based on its quantile values and the exposure map; thus, a 10 count limit at the aim point translates to a flux limit $F_x > 10^{-15}$ erg cm^{-2} s^{-1} over the whole field.

In DF1, we find 10.7% thermal sources, 53.3% soft-power-law-sources (of which 9% are obscured), and 35.7% hard-power-law-sources. Multiplying these percentages by the number (131) of sources down to our completeness limit yields 14 $\pm$ 6 thermal, 71 $\pm$ 17 soft-power-law, and 46 $\pm$ 13 hard-power-law-sources.

The same analysis of DF2 yields 10.5% thermal sources, 50% soft-power-law (of which 7.9% are obscured), and 39.5% hard-power-law-sources. Multiplying these percentages by the number (107) of sources down to our completeness limit yields 11 $\pm$ 6 thermal, 54 $\pm$ 16 soft-power-law, and 42 $\pm$ 14 hard-power-law.

An underlying assumption in extrapolating the ratios of high S/N sources to absolute numbers is that the luminosity functions of all three populations are the same over that range. Although this fact is unlikely to be true, we note that the fainter (S/N > 3) sources (top panels of Figure 20) appear to follow the same groupings as the high S/N examples. Therefore, we quote these quantile-based population numbers as a guide only. Determination of the nature of each individual source is being sought by a multi-wavelength survey, which will enable the actual luminosity functions to be determined for each species (HMXBs, stars, and AGNs, etc.), which is beyond the scope of this paper.

For comparison with the quantile results, we estimated the expected number of background AGNs in our survey based on the work of Kim et al. (2007). For the same flux limit of $F_x > 10^{-15}$ erg cm^{-2} s^{-1}, Kim et al.'s (2004) Figure 4 shows AGNs of order 10^3 per square degree. Thus, for an ACIS-I field of view ($16' \times 16'$), one expects to see $\sim$71 AGNs per field. The purpose of this comparison is to test whether the quantile results are reasonable in the light of what is known about the background AGN population. The quantile-derived AGN number is remarkably consistent with our prediction based on the AGN luminosity function of Kim et al. (2007). We note that DF2 contains a large X-ray bright SNR which likely explains the slightly (23%) lower AGN numbers in this field. Systematic errors were estimated by varying the boundary of the region in the quantile plane used to classify the AGN. Moving the boundary between Γ = 1.2–1.5 changed AGN versus XRB fractions by an insignificant amount compared to the statistical error. We note that CVs and LMXB are expected to occupy the same quantile parameter space as the AGN, due to their soft-power-law and/or hot thermal spectra. Given that our AGN count is consistent with predictions, there is not a great deal of room for additional source populations. Thus, we can tentatively constrain the total number of LMXB and CVs with soft spectra to be within the error bars of the AGN estimate.

Based on the above results, we find that the DF *Chandra* observations have detected a large population of point sources in the SMC, significantly in excess of the number of background AGNs.

8. CONCLUSIONS

We have presented the first results from deep (100 ks) *Chandra* observations of two fields in the SMC Bar. These observations reach a detection limit of $\sim 10^{-15}$ erg cm^{-2} s^{-1} (for five ACIS-I net counts). At the distance of the SMC (60 kpc), this corresponds to a luminosity of $L_X = 4.3 \times 10^{32}$ erg s^{-1} (for $\Gamma = 1$, $N_{\rm H} = 5 \times 10^{21}$ cm^{-2}).

We detected 19 HMXBs in the SMC *Chandra* DFs, including 11 previously known pulsars, 2 new pulsars, and 4 other HMXB candidates (this number includes only objects with X-ray variability, and/or association with *ROSAT* sources and optical counterparts). The previously ambiguous identification of two close pairs of HMXBs ((1) SXP892 = RX J0049.5-7310 and RX J0049.2-7311, (2) RX J0052.1-7319=SXP15.3 and CXOU J005215.4-731915) has been resolved thanks to *Chandra*'s spatial resolution. The two newly discovered pulsars were in outburst, and their periods were measurable to a high degree of accuracy. We have therefore assigned the names SXP892 and SXP326 following the convention used by the SMC *RXTE* monitoring project (L05; G08). Three other sources showed periodic modulation (significance >95%), one of these (CXOU J005446.3-722523) has a period of $\sim$4600 s, a bright early-type optical counterpart, and hard X-ray quantiles, strongly suggesting an HMXB. Additional HMXB candidates were detected with sufficient S/N to place them unambiguously on the quantile diagram (Figure 20) in the region inhabited by pulsars, in tight agreement with the power-law spectral model ($\Gamma = 1$, $n_H \sim 10^{21}$) characteristic of SMC pulsars. We are confident in the identification of the three HMXB candidates (CXOU J005057.1-731008 = RX J0050.9-7310, CXOU J005215.4-731915, and CXOU J005352.5-722639) which were identified by the combined evidence of X-ray spectral properties, other X-ray catalogs, and positional association with bright early-type stars and emission-line objects (MA93).

There are in total 40 *Chandra* sources (17 in DF1, 23 in DF2) with bright stellar counterparts. Currently, 21 out of these 40 have been identified as confirmed or probable HMXBs, due to pulsation, X-ray variability (the 19 HMXBs mentioned above), and/or optical emission lines (providing two additional candidates). The published photometric data show that a further 12 counterparts occupy the same range of optical magnitude and $B-V$ color as the confirmed HMXBs and are consistent with early-type (<B3) stars. These objects likely include HMXBs, shocked-wind early-type stars, and colliding-wind binaries, pending a comprehensive analysis to be published in a companion paper (VA10). A comparable study by Naze et al. (2004) using *Chandra* and *XMM-Newton* observations of NGC 346, a young open star cluster which lies on the outskirts of the SMC's Bar, revealed 97 point sources. Based on hardness ratios and bright-star counterparts, the majority were proposed to be HMXBs, although none has yet been seen in a bright outburst state.

By detecting 8 of the 10 pulsars for which there are ephemerides, with 6 of them outside of their normal orbital phase range for X-ray outbursts, we have demonstrated that a significant fraction (at least 60%) of these systems have appreciable accretion driven X-ray emission during quiescence. To these six confirmed "quiescent-activity" pulsars, we can add the three candidates as quiescent or persistent low-luminosity HMXBs, whose 2–10 keV luminosities are substantially lower than normal Be-pulsar outbursts. The faintest confirmed Be-pulsar was SXP342, at $L_X = 3.8 \times 10^{33}$ erg s^{-1}, while the candidate Be-HMXB CXO J005352.5-722693 (Section 5.16) was detected at $L_X = 5.2 \times 10^{32}$ erg s^{-1}. Future efforts should be directed at increasing the number of HMXBs with orbital ephemerides and extending the sample to cover the persistent low-luminosity population.

The new sample of pulsars is consistent with a population about twice the size of the known "active" pulsar population regularly seen by *RXTE*. It is possible that some of these pulsars are HMXBs in a perpetually low-luminosity state, similar to the Galactic HMXB X Persei and its brethren (Delgado-Marti et al. 2001). The X-ray luminosity of X Per varies, but is seldom above $L_x = 10^{35}$ erg s^{-1}. The theoretical work of Okazaki & Negueruela (2001) informs us that Be/NS systems with low orbital eccentricity accrete at a very low, almost constant rate. The Be star's circumstellar disk in such systems is permanently tidally truncated (at the 3:1 resonance) well within the NS's orbital radius, except during large mass ejections from the star (the assumed cause of type II "giant" outbursts). X-ray pulsars with very short (less than a few seconds) periods that remain in the propellor regime probably also contribute to the quiescent population.

The complete source catalog (Table 2) is available online in electronic form, it contains positions, count rates, fluxes, and quantiles for 394 X-ray sources (211 in DF1 and 183 in DF2).

This is the first of a series of papers that address the very faint X-ray source population in the SMC, in particular the X-ray luminosity function of HMXBs, and a search for CVs, stars, and LMXBs in this low-metallicity dwarf galaxy.

We thank J. McDowell, V. Kalogera, and M. Smith for their expert input which made the *Chandra* observations possible. We also thank the referee for improving the manuscript. This work has been partly supported by NASA LTSA Grant NAG5-13056 and *Chandra* grant GO6-7087A. S.L. thanks Gemini Observatory for supporting this research. Gemini is operated by the Association of Universities for Research in Astronomy, Inc., on behalf of the international Gemini partnership of Argentina, Australia, Brazil, Canada, Chile, the United Kingdom, and the United States of America.

REFERENCES

Antoniou, V., Zezas, A., Hatzidimitriou, D., & McDowell, J. C. 2009, ApJ, 647, 1695
Bhattacharya, D., & van den Heuvel, E. P. J. 1991, Phys. Rep., 203, 1
Bildsten, L., et al. 1997, ApJS, 113, 367
Buccheri, et al. 1983, A&A, 128, 245
Buckley, D. A. H., Coe, M. J., Stevens, J. B., van der Heyden, K., Angelini, L., White, N., & Giommi, P. 2001, MNRAS, 320, 281
Campana, S., Gastaldello, F., Stella, L., Israel, G. L., Colpi, M., Pizzolato, F., Orlandini, M., & Dal Fiume, D. 2001, ApJ, 561, 924
Cleveland, W. S. 1981, Am. Stat., 35, 54
Coe, M. J., Edge, W. R. T., Galache, J. L., & McBride, V. A. 2005, MNRAS, 356, 502
Corbet, R. H. D. 1984, A&A, 141, 91
Corbet, R. H. D., Coe, M. J., Edge, W. R. T., Laycock, S., Markwardt, C. B., & Marshall, F. E. 2004, ATel, 277
Crampton, D., Hutchings, J. B., & Cowley, A. P. 1978, ApJ, 223, L79
Delgado-Marti, H., Levine, A. M., Pfahl, E., & Rappaport, S. A. 2001, ApJ, 546, 455
Edge, W. R. T. 2005, PhD thesis, Univ. of Southampton
Edge, W. R. T., Coe, M. J., Galache, J. L., McBride, V. A., Corbet, R. H. D., Markwardt, C. B., & Laycock, S. 2004, MNRAS, 353, 1286
Eger, P., & Haberl, F. 2008, A&A, 485, 807
Filipovic, M. D., Pietsch, W., & Haberl, F. 2000, A&A, 361, 823
Frank, J., King, A., & Raine, D. 2002, Accretion Power in Astrophysics (3rd ed.; Cambridge: Cambridge Univ. Press)
Galache, J. L., Corbet, R. H. D., Coe, M. J., Laycock, S., Schurch, M. P. E., Markwardt, C., Marshall, F. E., & Lochner, J. 2008, ApJS, 177, 189
Grimm, H. J., Gilfanov, M., & Sunyaev, R. 2003, MNRAS, 339, 793
Haberl, F., Eger, P., & Pietsch, W. 2008, A&A, 489, 327
Haberl, F., Filipovic, M. D., Pietsch, W., & Kahabka, P. 2000, A&AS, 142, 41
Haberl, F., & Pietsch, W. 2004, A&A, 414, 667
Haberl, F., & Pietsch, W. 2005, A&A, 438, 221
Haberl, F., Pietsch, W., Schartel, N., Rodriguez, P., & Corbet, R. H. D. 2004, A&A, 420, 19
Haberl, F., & Sasaki, M. 2000, A&A, 359, 573
Harris, J., & Zaritsky, D. 2004, AJ, 127, 1531
Hellier, C. 1994, MNRAS, 271, L21
Hilditch, R. W., Howarth, I. D., & Harries, T. J. 2005, MNRAS, 357, 304
Hong, J., Schlegel, E. M., & Grindlay, J. E. 2004, ApJ, 614, 508
Hong, J., van den Berg, M., Schlegel, E. M., Grindlay, J. E., Koenig, X., Laycock, S., & Zhao, P. 2005, ApJ, 635, 907
Hong, J., van den Berg, M., Schlegel, E. M., Grindlay, J. E., Koenig, X., Laycock, S., & Zhao, P. 2009, ApJ, 706, 223
Ikhsanov, N. R. 2006, MNRAS, 375, 698
Illarionov, A. F., & Sunyaev, R. A. 1975, A&A, 39, 185
in't Zand, J. J. M., Swank, J., Corbet, R. H. D., & Markwardt, C. B. 2001, A&A, 380, L26
Karino, S. 2007, PASJ, 59, 961
Kim, D.-W., et al. 2004, ApJS, 150, 19
Kim, M., Wilkes, B. J., Kim, D.-W., Green, P. J., Barkhouse, W. A., Lee, M. G., Silverman, J. D., & Tananbaum, H. D. 2007, ApJ, 659, 29
Koenigsberger, G., Georgiev, L., Moreno, E., Richer, M. G., Toledano, O., Canalizo, G., & Arrieta, A. 2006, A&A, 458, 513
Laycock, S., Corbet, R. H. D., Coe, M. J., Marshall, F. E., Markwardt, C., & Edge, W. R. T. 2003, MNRAS, 339, 435
Laycock, S., Corbet, R. H. D., Coe, M. J., Marshall, F. E., Markwardt, C., & Lochner, J. 2005, ApJS, 161, 96
Laycock, S., & Drake, J. 2009, ApJ, 701, 12
Leahy, D. A., Elsner, R. F., & Weisskopf, M. C. 1984, ApJ, 272, 256
Marshall, F. E., Lochner, J. C., & Takeshima, T. 1997, IAU Circ., 6777, 2
McBride, V. A., Coe, M. J., Negueruela, I., Schurch, M. P. E., & McGowan, K. E. 2008, MNRAS, 388, 1198
McBride, V. A., et al. 2007, MNRAS, 382, 743
McGowan, K., Coe, M. J., Corbet, R., Galache, J., & Laycock, S. 2007, MNRAS, 376, 759
McGowan, K. E., Coe, M. J., Schurch, M. P. E., Corbet, R. H. D., Galache, J. L., & Udalski, A. 2008, MNRAS, 384, 821
Meyssonnier, N., & Azzopardi, M. 1993, A&AS, 102, 451
Naze, Y., Manfroid, J., Stevens, I. R., Corcoran, M. F., & Flores, A. 2004, ApJ, 608, 208
Negueruela, I. 1998, A&A, 338, 505
Okazaki, A. T., & Negueruela, I. 2001, A&A, 377, 161
Parmar, A. N., White, N. E., & Stella, L. 1989, ApJ, 338, 373
Press, W. H., Flannery, B. P., Teukolsky, S. A., & Vetterling, W. T. 1992, Numerical Recipes (Cambridge: Cambridge Univ. Press)
Sasaki, M., Haberl, F., & Pietsch, W. 2000, A&AS, 147, 75
Scargle, J. D. 1982, ApJ, 263, 835
Schwarzenberg-Czerny, A. 1996, ApJ, 460, L107
Shtykovskiy, P., & Gilfanov, M. 2005, MNRAS, 362, 879
Stanimirovic, S., Staveley-Smith, L., Dickey, J. M., Sault, R. J., & Snowden, S. L. 1999, MNRAS, 302, 417
Stella, L., White, N. E., & Rosner, R. 1986, ApJ, 308, 669
Taylor, P., Zezas, A., McDowell, J. C., Hatzidimitriou, D., Kalogera, V., & Fabbiano, G. 2003, BAAS, 35, 1396
Urpin, V., Konenkov, D., & Geppert, U. 1998, MNRAS, 299, 73
Yokogawa, J., Imanishi, K., Tsujimoto, M., Koyama, K., & Nishiuchi, M. 2003, PASJ, 55, 161
Yokogawa, J., Imanishi, K., Ueno, M., & Koyama, K. 2000, PASJ, 52, L73
Young, M. D., Manchester, R. N., & Johnston, S. 1999, Nature, 400, 848
Zaritsky, D., Harris, J., Thompson, I. B., Grebel, E. K., & Massey, P. 2002, AJ, 123, 855